Exp Fluids (2009) 46:1–26
DOI 10.1007/s00348-008-0582-5

REVIEW ARTICLE

Single dielectric barrier discharge plasma enhanced aerodynamics: physics, modeling and applications

Thomas C. Corke · Martiqua L. Post · Dmitriy M. Orlov

Received: 15 March 2008 / Revised: 16 October 2008 / Accepted: 17 October 2008 / Published online: 16 November 2008
© Springer-Verlag 2008

Abstract The term "plasma actuator" has been a part of the fluid dynamics flow control vernacular for more than a decade. A particular type of plasma actuator that has gained wide use is based on a single dielectric barrier discharge (SDBD) mechanism that has desirable features for use in air at atmospheric pressures. For these actuators, the mechanism of flow control is through a generated body force vector that couples with the momentum in the external flow. The body force can be derived from first principles and the plasma actuator effect can be easily incorporated into flow solvers so that their placement and operation can be optimized. They have been used in a wide range of applications that include bluff body wake control; lift augmentation and separation control on a variety of lifting surfaces ranging from fixed wings with various degrees of sweep, wind turbine rotors and pitching airfoils simulating helicopter rotors; flow separation and tip-casing clearance flow control to reduce losses in turbines, to control flow surge and stall in compressors; and in exciting instabilities in boundary layers at subsonic to supersonic Mach numbers for turbulent transition control. New applications continue to appear through programs in a growing number of US universities and government laboratories, as well as in Germany, France, England, Netherland, Russia, Japan and China. This paper provides an overview of the physics, design and modeling of SDBD plasma actuators. It then presents their use in a number of applications that includes both numerical flow simulations and experiments together.

T. C. Corke (✉)
Aerospace and Mechanical Engineering Department,
Center for Flow Physics and Control, University of Notre Dame,
Notre Dame, IN, USA
e-mail: tcorke@nd.edu

M. L. Post · D. M. Orlov
US Air Force Academy, Colorado Springs, CO, USA

List of symbols

C	capacitance
C_D	drag coefficient
C_L	lift coefficient
D	drag force
E	electric field
E_b	breakdown electric field
E_s	sustaining electric field
F^+	reduced frequency = fL_{sep}/U_∞
I	current
I_c	conduction current
I_d	displacement current
L	lift force
L_{sep}	streamwise extent of separation region
P	power
R	resistance
Re_c	Reynolds number based on chord length and free-stream velocity
T	period of ac cycle
T_{max}	maximum thrust
U	mean streamwise velocity
U_∞	free-stream velocity
u'	root-mean-square of streamwise velocity fluctuations
V	plasma actuator voltage
V_{ac}	ac voltage
V_{p-p}	ac peak-to-peak voltage
c	wing chord
f_{ac}	ac excitation frequency of unsteady plasma actuator
f_b	body force
q	dynamic pressure

rf	radio frequency
x, y	axial coordinates
t	time
α	angle of attack
α_s	stall angle of attack
$\alpha_{0\ L}$	zero lift angle of attack
ε_0	universal charge in a vacuum
λ_D	Deby length
ϕ	phase shift
ω	$2\pi/f_{ac}$
ρ_c	charge density
φ	electric potential

1 Background

Interest in dielectric barrier discharges (DBD) "plasma actuators" for flow control has seen a tremendous growth in the past ten years in the US and around the world. The reasons for this are likely based on their special features that include being fully electronic with no moving parts, having a fast time response for unsteady applications, having a very low mass which is especially important in applications with high g-loads, being able to apply the actuators onto surfaces without the addition of cavities or holes, having an efficient conversion of the input power into fluid momentum (Enloe et al. 2004b; Post 2001; Post 2004), and the easy ability to simulate their effect in numerical flow solvers (Corke et al. 2006a). Details for these claims are covered in a discussion of the plasma actuator physics in Sect. 2.

The DBD plasma actuators consist of two electrodes, one exposed to the air and the other covered by a dielectric material. An example configuration is shown in Fig. 1. The electrodes are supplied with an ac voltage that at high enough levels, causes the air over the covered electrode to ionize. In the classic description, the ionized air is a "plasma," which is why these are referred to as

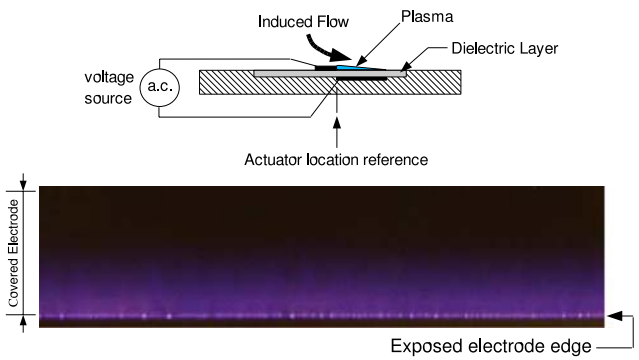

Fig. 1 Schematic illustration of SDBD plasma actuator (*top*) and photograph of ionized air at 1 atm. pressure that forms over electrode covered by dielectric layer (*bottom*)

"plasma actuators" (Cavalieri 1995; Corke et al. 2001; Corke and Matlis 2000). The ionized air appears blue (Davidson and O'Neil 1964). The emission intensity is extremely low, requiring a darkened space to view by eye. The plasma is captured in the photograph in the bottom part of Fig. 1.

The ionized air, in the presence of the electric field produced by the electrode geometry, results in a body force vector that acts on the ambient (neutrally charged) air. The body force is the mechanism for active aerodynamic control. If operated optimally, there is very little heating of the air (Iqbal et al. 2007; Orlov 2006). The underlying physics behind their operation will be discussed in detail in later sections.

The word "plasma" was introduced into the physics literature by Langmuir (1926) to denote an electrically neutral region of gas discharge. This definition has in time been broadened and now refers to a system of particles whose collective behavior is characterized by long-range coulomb interactions (Kunhardt 2000). One description typically added to highlight another property of plasmas is "collisional", where the electron-neutral collision frequency is of the order of, or greater than, the plasma frequency. This is a property of the regime that is relevant to the DBD plasma actuators.

A gas discharge is created when an electric field of sufficient amplitude is applied to a volume of gas to generate electron-ion pairs through electron impact ionization of the neutral gas (Kunhardt 1980; Kunhardt and Luessen 1981; LLewellyn-Jones 1966; Raizer 1991). This requires the presence of an initiating number of free electrons which can either be present from ambient conditions, or introduced purposely (Kunhardt 1980; Kunhardt and Luessen 1981).

A traditional (industrial) arrangement for creating a self-sustained gas discharge at low pressures of a few Torr or less has involved separated facing electrodes. The electric field established by the two electrodes can either be by direct current (dc) or alternating current (ac). The plasma is generated by increasing the amplitude of the electric field above the breakdown electric field, E_b, which is the value needed to sustain electron-ion pairs in the gas in the absence of space-charge fields (Kunhardt 1980; Kunhardt and Luessen 1981; LLewellyn-Jones 1966; Raizer 1991). The minimum breakdown electric field is a function of the driving frequency. At atmospheric pressure, E_b is generally lower for an ac input. The optimum ac frequency depends on the static pressure and the particular gas. Once created, the electric field needed to sustain the plasma, E_s, is lower than E_b. The difference between the breakdown and sustaining electric fields is a function of the operating conditions (Llewellyn-Jones 1966; Raizer 1991; Nasser 1971; Meek and Craggs 1978).

As a consequence of the plasma conductivity, there is a current, I, that flows between the electrodes. A region is formed between the plasma and the cathode electrode whose role is to provide current continuity at this interface. The current in the boundary region consists of two components: the conduction current, I_c, and the displacement current, I_d. For dc fields, I_d is zero, and the remaining conduction current consists of electron and ion components. For ac fields, the contribution of the displacement current to the total current increases with frequency.

When the operating conditions (applied field, electrode cross-section area, and static pressure) are such that the current density in the boundary region near the cathode is independent of the current flowing in the circuit, the discharge is called a "normal glow discharge" (LLewellyn-Jones 1966; Raizer 1991; Kunhardt and Luessen 1981; Nasser 1971; Meek and Craggs 1978). For constant current, the current density in a normal glow discharge scales with the square of the static pressure. Therefore the cross-section area of plasma decreases with increasing pressure at constant current. As the static pressure increases at constant current, the current density increases until the threshold for the development of instabilities leading to a transition to an "arc" phase is reached. The threshold current for the development of the "glow-to-arc" transition depends on the operating conditions of the discharge.

Many aerodynamic flow control applications would require plasma actuators to operate near atmospheric pressure. This favors ac operation over dc. In addition, any gains they might provide in efficiency need to factor in the power they require to operate. Thus there is a need to consider their most efficient operating conditions that maximize their effect with respect to input power.

A technique for generating steady-state, high-pressure diffuse plasmas uses a dielectric barrier on the surface of one or both electrodes. An early reference to this approach is due to Okazaki and co-workers (Kanazawa et al. 1988, 1989, 1990; Yokoyama et al. 1990; Okazaki et al. 1993; Kogoma and Okazaki 1994). In this case because of the dielectric layer, the electrodes must be supplied with an ac field. Barrier-electrode discharges have been operated historically in the "micro-discharge" mode (Eliasson and Kogelschatz 1991; Kogelschatz 1977). In this mode, the discharge consists of a number of parallel filaments, each of which have a limited lifetime. The filaments are essentially streamer discharges whose lifetime is governed by the capacitance of the dielectric barrier (Eliasson and Kogelschatz 1991). The passage of the streamer across the discharge gap locally charges this capacitance, reversing the local field and thus terminating the filament.

In sinusoidally driven DBD, the plasma forms in "non-thermal equilibrium," in which the electrical energy coupled into the gas is mainly used to produce energetic electrons while the gas remains at ambient temperature. This is due to the self-termination of the discharge which prevents micro-discharges from degenerating into a thermal arcs (Falkenstein and Coogan 1997). The process of self-termination results from the accumulation of electrons at the dielectric surface facing the cathode. The internal electric field caused by the accumulation of electrons on the dielectric surface reduces the local field strength, and the micro-discharges choke themselves as the extinction field is reached (Falkenstein and Coogan 1997).

For a single dielectric barrier discharge (SDBD), during one-half of the ac cycle, electrons leave the metal electrode and move towards the dielectric where they accumulate locally. In the reverse half of the cycle, electrons are supplied by surface discharges on the dielectric and move toward the metal electrode. The time scale of the process depends on the gas composition, excitation frequency and other parameters. In air at atmospheric pressure, it occurs within a few tens of nanoseconds (Falkenstein and Coogan 1997).

Kline et al. (2001) have studied time-resolved images of spatio-temporal patterns in a one-dimensional dielectric-barrier discharge system. They obtained images of plasma filaments that revealed "discharge stages" that lasted only approximately 100 ns. They found that several discharge stages could occur during a half-cycle of the driving oscillation, each producing a distinct filament pattern. They found that in some discharges there was a temporal structure but spatial disorder, and in others there was both temporal and spatial disorder in the discharges.

The dielectric barrier configuration will also support a uniform diffuse discharge operation as shown by Okazaki (Kanazawa et al. 1988). The mechanisms that play a role in this are well understood from a number of investigators (Roth 1995a; Decomps et al. 1994; Massines et al. 1995; Trunec et al. 1998; Massines et al. 1998b). The stability of the diffuse mode depends on the ac frequency, the gas type and the excitation power. The discharge is most stable in Helium and mixtures that contain Helium, although other gases have been used including air (Kanzawa et al. 1990; Roth 1995a; Decomps et al. 1994; Massines et al. 1995, 1998; Trunec et al. 1998). The electrode separation is usually small, of the order of a few centimeters. The electron density of the plasma generated by this mode is of the order of 10^{10} cm^{-3}.

Radio frequency (rf) glow discharges are used in micro-electronic device fabrication and gas laser excitation. For high pressure gas laser excitation, dielectric-covered electrodes are particularly employed to achieve higher stability and homogeneity compared to metallic electrodes with dc discharges (Kakuta et al. 1995). In industrial systems, the

rf discharge is driven at 13.56 MHz which is the value regulated by the Federal communication commission (FCC). Optical emission spectroscopy of rf discharges is one of the conventional and nonintrusive diagnostic techniques used to study barrier discharges of this type. Boeuf (1987) provided one of the earlier models for rf glow discharges of this type.

A one-dimensional model for the dielectric barrier discharge dynamics was developed by Massines et al. (1998a), Rabehi et al. (1994) and BenGadri et al. (1994). It was based on the numerical solution of the electron and ion continuity and momentum transfer equations coupled to Poisson's equation. As is typical in high pressure discharges, the electrons and ions were assumed to be in equilibrium with the electric field. Their model gave space and time variations in the electric field, and the electron and ion densities. The charge accumulation on the dielectric as the discharge develops was taken into account, and the voltage boundary conditions for dielectrics were derived by considering an equivalent circuit of the gas gap in series with the equivalent capacitor of the dielectric.

One of the earliest uses of plasma actuators for flow control was by Kosinov et al. (1990) to excite Tollmein-Schlichting (TS) modes in a Mach 2.0 boundary layer over a flat plate. The plasma was formed between two electrodes located in a cavity below the plate surface. The driving ac frequency was selected to be in the range of the most amplified TS frequency. This provided a phase reference from which streamwise and spanwise wavelengths of the amplified disturbances could be derived. With a similar intent, Cavalieri (1995) and Corke et al. (2001) used an azimuthal array of plasma actuators on the surface of a sharp-tipped circular cone in a Mach 3.5 flow. The ac input to the individual electrodes was phase shifted to excite particular azimuthal wave numbers of Tollmien-Schlichting (TS) modes in the boundary layer.

In one of the earliest low-speed applications, Roth, Sherman and Wilkinson (Roth et al. 1998, 2000) utilized an array of electrodes separated by a glass-epoxy printed-circuit board to manipulate the boundary layer flow over a flat plate at free-stream velocities from 4 to 26 m/s. They investigated a number of electrode geometries. One of these was similar to the one shown in Fig. 1. With this electrode configuration, they observed using smoke visualization that ambient air was drawn towards the covered electrode. A similar photograph recorded by Post (2001) is shown in Fig. 2. In this case, the electrodes are aligned parallel to the mean flow direction. This accentuates the width of the streamtube that is drawn towards the wall by the actuator. Velocity surveys of the actuator induced flow by Roth et al. (1998b, 2000) documented a wall-normal mean velocity profile that was similar to what might be produced by a tangential wall jet.

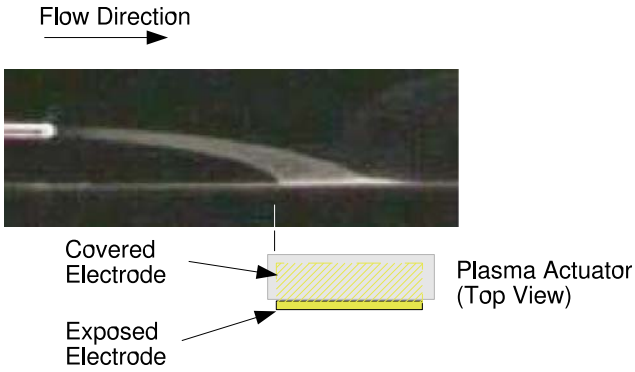

Fig. 2 Photograph of smoke tube introduced at the edge of a boundary layer that is bent towards the wall by a plasma actuator oriented so that the electrodes are parallel the streamwise direction. (from Post 2001)

Corke and Matlis (2000) investigated an array of SDBD plasma actuators that were phased to produce a traveling wave effect. It was applied to a flat surface as well as to the inside wall of a circular nozzle where it was used to excite helical instability modes in a jet flow. Post 2001 and Post et al. 2001 used the flat surface array to study its effect on the wall in a turbulent boundary layer. Later Hultgren and Ashpis (2003) utilized a similar phased-array approach for separation control in an adverse pressure gradient simulation of a low-pressure turbine blade.

Following this early development, the design of the SDBD plasma actuator has primarily settled on the asymmetric electrode geometry used either singly, or in linear arrays. As part of a fundamental study on plasma actuators of this geometry, Post (2004) documented the flow induced by a single actuator in still air using both particle image velocimetry (PIV) and Pitot probes. Velocity vectors obtained using PIV are shown in Fig. 3. The actuator was operated by supplying separate ac inputs to the exposed and covered electrodes. The frequencies of the two ac inputs differed by 1 Hz. This produced an ac potential across the electrodes that was amplitude modulated at the difference frequency. As a result, the actuator smoothly turned on an off with a period of 1 s. A trigger signal was constructed from the modulated amplitude and used to phase-lock velocity ensembles from the PIV system. Figure 3 shows four such ensemble averages corresponding to modulation period phase angles of $\phi = 0$, 90, 180 and 270°. The edge of the exposed electrode facing the covered electrode is located at $x = -26$ mm in the plots.

At $\phi = 0$ (top-left plot) the actuator is just being activated. Just upstream of the actuator location, the velocity vectors are directed towards the wall. This is visible in all of the plots at all of the phase angles, and is consistent with the downward-bent smoke streakline that was observed upstream of the plasma actuator by Roth et al. 1998b, 2000

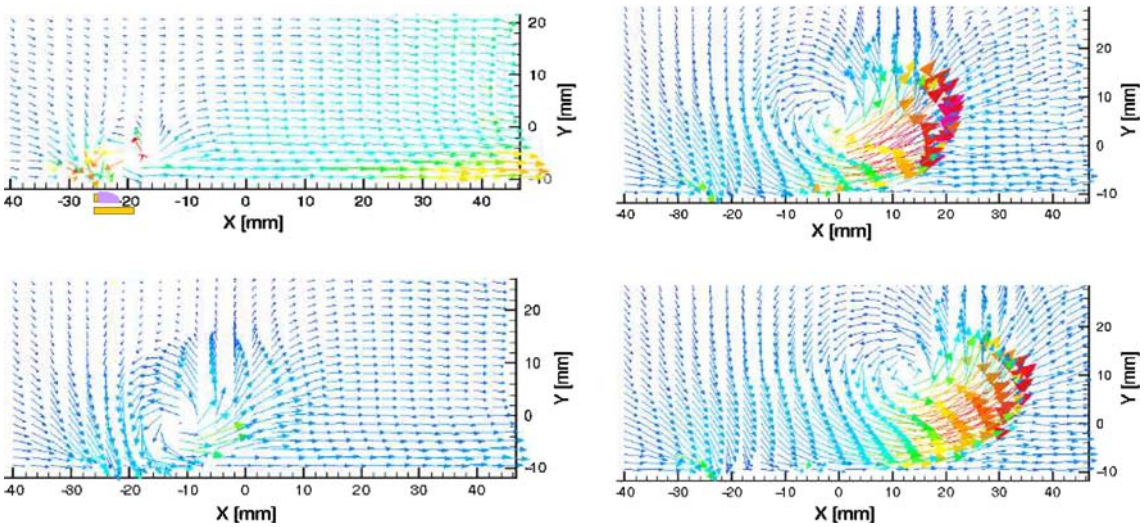

Fig. 3 Ensemble-averaged velocity vectors obtained using PIV that illustrate the flow induced by an SDBD plasma actuator like that illustrated in Fig. 1 in still air. Vector plots (from *top-left* to *bottom-right*) correspond to phase angles of 0, 90, 180, and 270° of a 1 Hz amplitude-modulated input. (from Post 2004)

and Post 2001. Close to the wall, the vectors indicate that the flow is accelerating and moving parallel to the wall in the direction away from the actuator. Because the actuator is in still air, the initiation of the plasma produces a "starting vortex" similar to an impulsively moved wall. The velocity vectors at subsequent phase angles document the vortex as it convects out of the measurement area. The last remnant of it is observed in the vectors near the far-right boundary at $\phi = 0$ (top-left plot).

Post and Corke (2004) compiled the PIV velocity data to construct a wall-normal profile of the velocity component parallel to the wall (U). This is shown in Fig. 4. Included as a check are two sets of measurements obtained using a pitot probe. The dashed curve is from an early simulation of the actuator that will be discussed in a later section.

These results serve to denote the fundamental features of asymmetric-electrode SDBD plasma actuators, namely:

1. an induced net downward flow towards the edge of the exposed electrode in the direction of the covered electrode, and
2. a jetting of the flow towards the far edge of the covered electrode.

The physics of its operation and how it might be optimized, is the topic of the following sections.

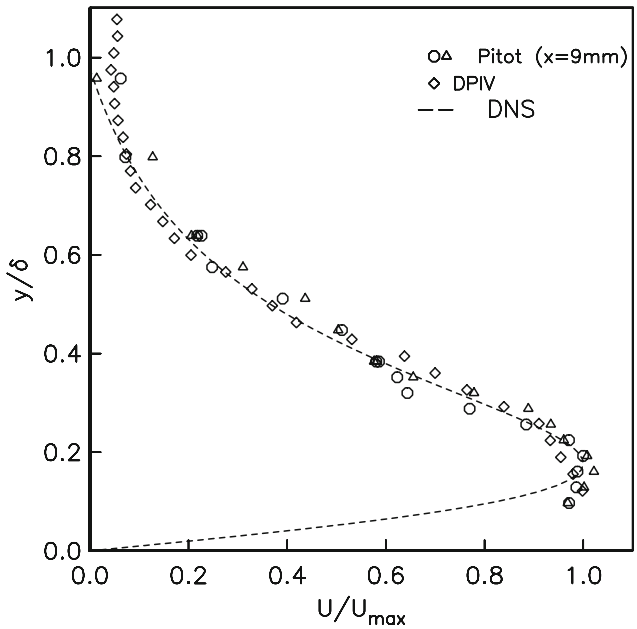

Fig. 4 Mean velocity profiles of the velocity component parallel to the wall (U) of flow induced by an asymmetric-electrode SDBD plasma actuator like that illustrated in Fig. 1 in still air (from Post and Corke 2004)

2 SDBD actuator physics

This section examines the physics behind the SDBD plasma actuator configurations that are most commonly used in flow control. Although dielectric-barrier discharge plasma generators have been used for many years for industrial purposes (Roth 1995), they generally use facing plate electrodes, and operate with gases other than air and at low pressures well below atmospheric. The need for flat configurations that can be placed on a single surface in air at near atmospheric pressures makes their operation somewhat different from the classic industrial DBD plasma generators in the literature.

2.1 Experimental observations

The SDBD plasma actuators are driven by an ac input. In classic DBD processes, the input waveform is sinusoidal. When the ac amplitude is large enough so that the electric field exceeds E_b, the air ionizes. The ionized air is always observed to form over the electrode that is covered by the dielectric. In addition to the unaided eye, the ionized air appears to be uniform in color and distribution. The photograph in Fig. 1 is a typical example. Time resolved images of the ionization process however indicate it to be a highly dynamic, spatially evolving process with features that develop on the time scale of the ac period (mili-seconds) or less.

Enloe et al. (2004a) studied the space-time evolution of the ionized air light emission over a surface mounted SDBD plasma actuator using a photo-multiplier tube (PMT) fitted with a double-slit aperture to focus on a narrow 2-D region of the plasma. The slit was parallel to the edge of the exposed electrode and could be moved to different locations over the electrode covered by the dielectric. A similar arrangement was done by Orlov (2006), a schematic of which is shown in Fig. 5.

A sample time series from Orlov (2006) of the PMT output that was acquired phase-locked with the ac input to the actuator is shown in Fig. 6. Also shown for reference is the ac input supplied to the electrodes. The light emission is taken as an indication of the plasma density, which is a good assumption based on the disparate time scales between the recombination time (order of 10^{-8} s) (Vidmar and Stalter 2003) versus the discharge time scale (order of 10^{-3} s).

There are several fundamental features of light emission time series. The first is that the air is ionized only over part of the ac cycle. When it does ionize, its character is different between the first and second halves of the ac cycle. This is the second fundamental feature. The final fundamental feature is that the light emission is made up of narrow spikes that might indicate numerous micro-

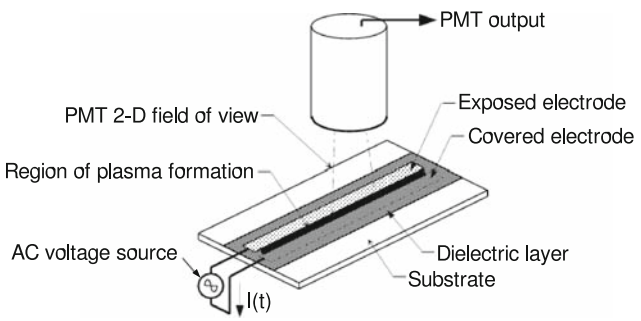

Fig. 5 Photo-multiplier arrangement for documenting the space-time evolution of ionized air light emission over the dielectric surface of SDBD plasma actuator

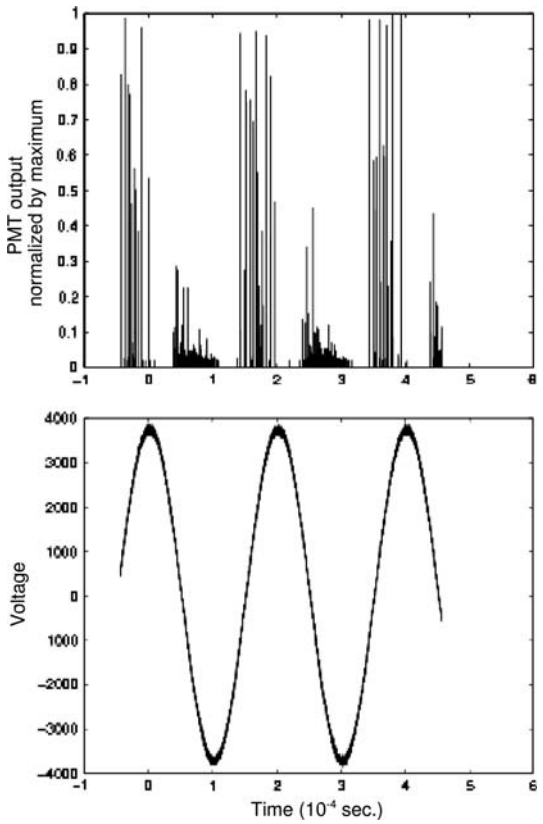

Fig. 6 Time series of PMT output (*top*) that is viewing ionized air light emission at one location over electrode covered by dielectric, and corresponding ac input (*bottom*) to plasma actuator (from Orlov 2006)

discharges. Similar observations have been documented by Enloe et al. (2004a), Massines et al. (1998a), and Eliasson and Kogelschatz (1991) and Kogelschatz (1977), which generally characterize this process as a dielectric barrier discharge (DBD).

The most important property of the DBD is that it can sustain a large volume discharge at atmospheric pressure without the discharge collapsing into a narrow constricted electrical arc. This is governed by the build-up of charges on the dielectric surface. The process for this is illustrated in Fig. 7. The left part of the figure corresponds to the half cycle of the discharge where the exposed electrode is more negative than the surface of the dielectric covering the other electrode. In this case when the electric potential is large enough, electrons are emitted from the exposed electrode and deposited onto the dielectric surface. As the charge on the dielectric builds up, it opposes the applied voltage on the bare electrode. The discharge will eventually stop unless the magnitude of the applied voltage continues to increase. This is not the case for a periodic input in which the potential reverses. The blue rectangle shows the portion of the ac cycle where the air would ionize. This is initiated at (a) when the potential between the bare electrode and dielectric surface is large enough so

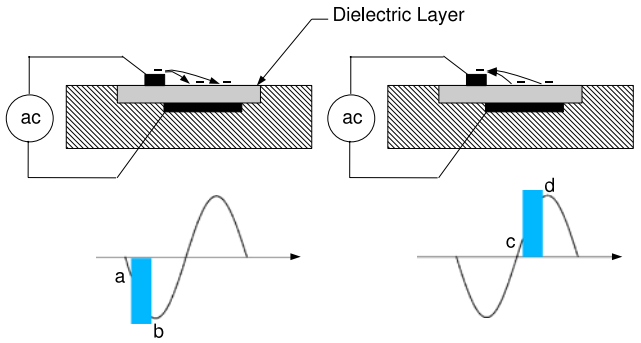

Fig. 7 Illustration of electron drift that dictates portions of ac period where air ionizes in SDBD process

that the electric field exceeds E_b. The ionization stops at (b) when the voltage on the bare electrode stops becoming more negative, which is needed to overcome the buildup of charge on the dielectric.

The behavior of the discharge is similar on the opposite half of the ac cycle which is illustrated on the right part of Fig. 7. In this case, the exposed electrode is more positive than the surface of the dielectric which is now holding the deposited electron charge. When the potential difference is large enough, the electrons will be emitted from the dielectric surface to the bare electrode (c). Again the blue rectangle shows the portion of the ac cycle where the air would ionize. The ionization stops (d) when the voltage at the bare electrode stops becoming more positive and the electric field falls below E_b.

Focusing back on light emission time series in Fig. 6, the air was ionized in the expected parts of the ac cycle. In addition, the time series indicates that the discharge is much more irregular in the positive-going half cycle than in the negative-going half cycle. This is consistent with the literature for DBDs with a single dielectric barrier (Gibalov and Pietsch 2000b; Pashaie et al. 1994), and was also observed by Enloe et al. (2004a). The explanation for the difference in the emission character in the two half-cycles is associated with the source of electrons. During the negative-going half cycle, the electrons originate from the bare electrode, which is essentially an infinite source that readily gives them up. In the positive-going half cycle, the electrons originate from the dielectric surface. These apparently do not come off as readily, or when they do, they come in the form of micro-discharges. This asymmetry plays an important role in the efficiency of the momentum coupling to the neutrals. It further suggests some optimization can come in the selection of the ac waveform to improve the performance of the plasma actuator. For example, a sawtooth with the long rise time corresponding to the portion of the ac period when the electric potential direction is depositing electrons on the dielectric has been show to produce more induced thrust when compared to sine waves (Enloe et al. 2004a). In general, triangle waves are more optimal than sine waves, and square waves or rectangular pulses are least favorable in ionizing the air for SDBD plasma actuators.

The light emission time series that was shown in Fig. 6 corresponded to observing a single narrow slit at a fixed location over the dielectric. A composite of light emission time series measured at different positions over the dielectric surface that were obtained by Orlov 2006 and Orlov et al. 2006 are shown in Fig. 8. These are shown as contours of constant light intensity for one period, T, of the ac cycle. The x axis is the distance over the covered electrode measured from the edge of the bare electrode at the interface of the covered electrode.

The space-time character of the plasma light emission over the covered electrode has a number of interesting features. For example, there is a sharp amplitude peak near the edge of the exposed electrode at the first initiation of the plasma. As time increases, the plasma sweeps out from the junction to cover a portion of the encapsulated electrode. This was similarly noted by Gibalov and Pietsch (2000a). As the plasma sweeps out away from the edge of the exposed electrode, its light emission appears to become less intense. Estimates (Enloe et al. 2004a; Orlov 2006; Orlov et al. 2006) indicate that the intensity decreases exponentially from the junction. This led to the use of an exponential weighting for correcting the spatial dependence of the plasma actuator body force in earlier flow simulations (Orlov et al. 2003; Orlov and Corke 2005; Voikov et al. 2004). Two of the global features of the

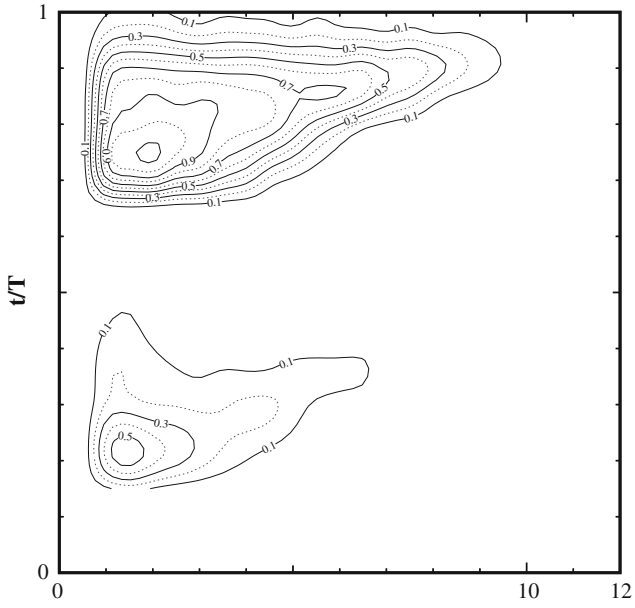

Fig. 8 Space-time variation of the measured plasma light emission for SDBD plasma actuator corresponding to one period, T, of the input ac cycle. (from Orlov 2006; Orlov et al. 2006)

space-time evolution of the plasma formation are the velocity at which the plasma front moves across the dielectric, and the maximum extent of the plasma during the ac cycle. The velocity is represented by the slope, dx/dt, of the front. In Fig. 6, the velocity of the fronts is approximately the same for the two halves of the ac cycle, but the plasma extent differs.

Enloe at al. (2004a) determined that the propagation speed of the discharge increased with the applied ac voltage. In addition they found that the propagation speed was essentially the same during the ionization that occurs in both halves of the ac cycle. On this basis, both halves of the ac cycle are equivalent.

Orlov (2006) investigated the effects of voltage and ac frequency on the extent and propagation velocity of the discharge. The effect of the input voltage level is shown in Fig. 9. The left plot corresponds to the maximum extent of the plasma as it sweeps out from the edge of the bare electrode onto the dielectric covered electrode. This indicates that the maximum extent varies linearly with the voltage amplitude. The right plot shows the velocity of the plasma front as a function of the applied voltage. Orlov (2006) determined the front velocity by measuring the slope, dx/dt, of the edge of the light-emission in contour plots like the one shown in Fig. 8. Enloe et al. (2004a) determined the front velocity by measuring the time delay to when the light emission was first observed in a viewing slit located various distances from the bare electrode edge. As a result of the larger amount of scatter, Enloe et al. (2004a) estimated that the plasma velocity was approximately constant with applied ac voltage. With somewhat less scatter, Orlov (2006) found it to increase with voltage. The line through the data is a linear curve that is the best fit to the combined sets of data. Also included in these two plots are the results from the lumped-circuit model of Orlov (2006) that is discussed in Sect. 2.2 on the SDBD Body Force Model.

The effect of the ac frequency on the extent and propagation velocity of the discharge is shown in Fig. 10. This result is taken from Orlov (2006). The left plot shows the plasma extent. Aside from the value at the lowest frequency, it indicates that there is no dependence of the plasma extent on the ac frequency. In contrast to this, the right plot indicates that the plasma velocity increases

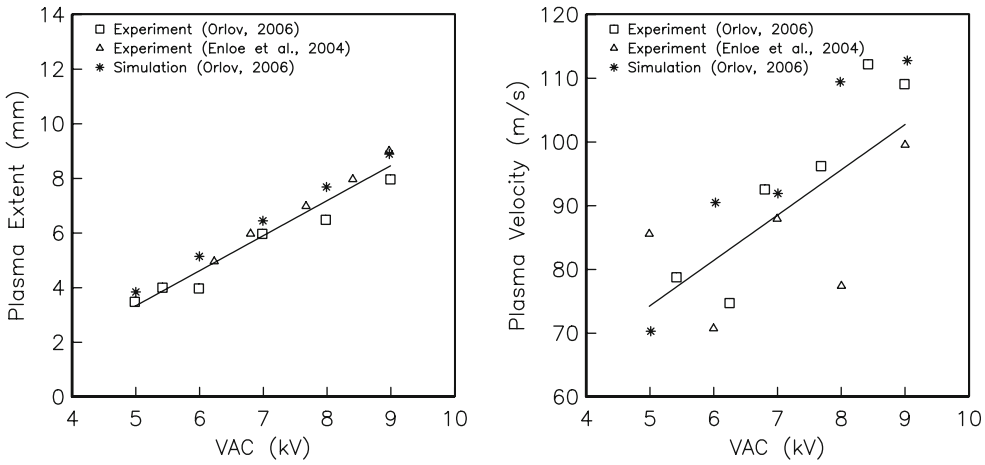

Fig. 9 Effect of input voltage on the extent (*left*) and velocity (*right*) of the plasma discharge edge for SDBD actuator. (from Orlov 2006; Orlov et al. 2006)

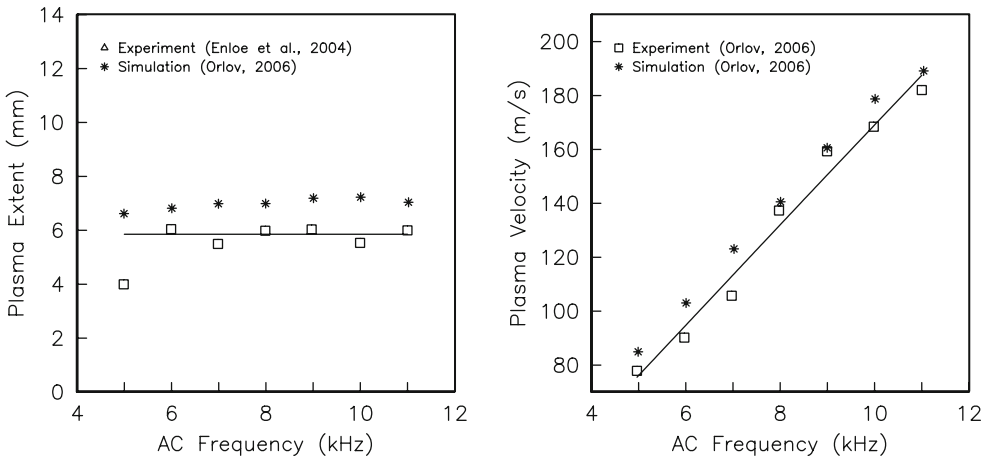

Fig. 10 Effect of input ac frequency on the extent (*left*) and velocity (*right*) of the plasma discharge edge for SDBD actuator. (from Orlov 2006; Orlov et al. 2006)

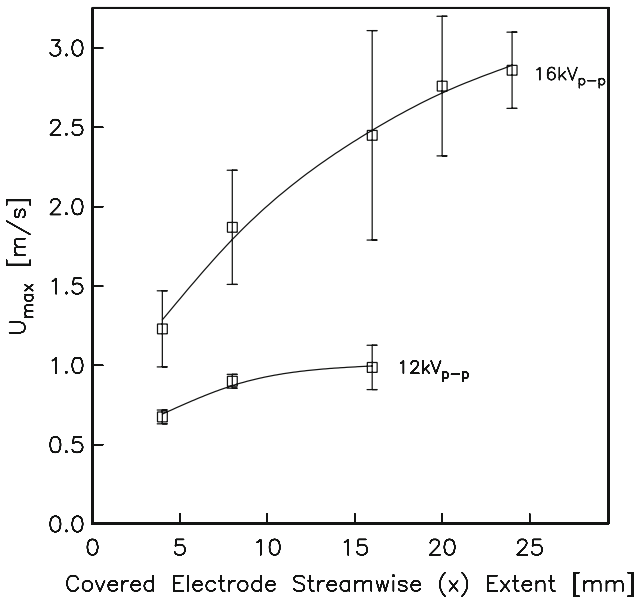

Fig. 11 Effect of covered electrode width on velocity induced by plasma actuator. (from Post 2004)

linearly with the ac frequency. The curve corresponds to a best fit straight line through the points. Since the extent of the plasma only depended on the voltage, these results indicated that as the ac frequency increased (corresponding to a decreasing ac period), the time needed for the plasma to reach its maximum extent within each half of the ac period decreased. Therefore, the propagation velocity of the plasma increased in proportion to the ac frequency. Results from the lumped-circuit model of Orlov (2006) that is discussed in Sect. 2.2 have been included in these two plots.

The results of these two figures has a direct implication on the design of the covered electrode. For example Post (2004) and Enloe et al. (2004b) showed that with increasing ac amplitude, the maximum velocity induced by the plasma actuator was limited by the streamwise (x) extent of the covered electrode. This is illustrated in Fig. 11 for two input voltages. Thus the dielectric area needed to store charge can be too small to take full advantage of the applied voltage.

The final aspect of the SDBD plasma actuator physics is the manner that it induces flow in the neutral air. As previously shown in Fig. 4, the asymmetric electrode configuration results in a flow with a velocity profile not unlike a wall jet. In their second paper, Enloe et al. (2004b) sought to correlate the magnitude of the induced flow by measuring the induced reaction thrust force acting on the actuator. This was done by mounting the actuator on a fulcrum to increase the resolution of the thrust so that it could be measured on an electronic force scale. A similar experiment was performed by Iqbal et al. (2007). The design of those actuators produced an order of magnitude larger thrust so that the force could be directly measured by mounting the actuator on an electronic scale. This is illustrated in the left part of Fig. 12. The right part of the figure shows the measured force as a function of the applied ac voltage.

The induced thrust versus voltage is plotted on log-log axes because the first measurements of Enloe et al. (2004b) indicated that the thrust force produced by the actuator was proportional to $V_{ac}^{3.5}$. The line through the data in Fig. 12 is the best fit of the function $T = C_1\, V^{3.5}$ to the data, where C_1 is the fitted parameter. This confirms the original observation. Post (2001, 2004) verified a similar dependence of the maximum velocity in the wall-normal profile. These measurements were performed at a sufficient distance from the edge of the bare electrode where the velocity profiles were verified to be self similar. Therefore the maximum velocity was consistent with the momentum in the induced flow found by integrating the velocity

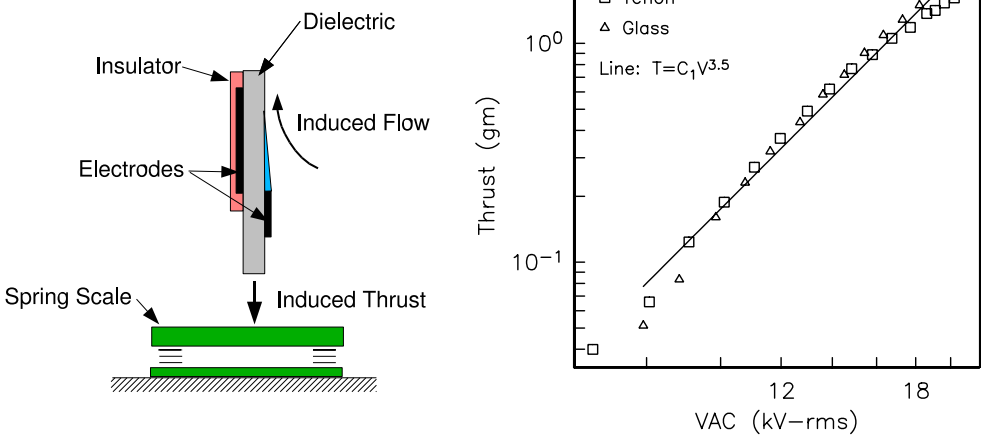

Fig. 12 Schematic of experimental setup for measuring induced thrust from SDBD plasma actuator (*left*) and measured thrust versus applied ac voltage (*right*). (from Iqbal et al. 2007)

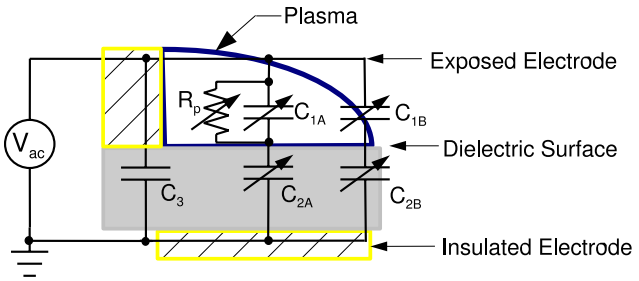

Fig. 13 Lumped element circuit model of the SDBD plasma actuator. (from Enloe et al. 2004a)

profile, which should equal the thrust. Iqbal et al. (2007) verified consistency between the momentum found by integrating the profiles and the measured thrust force.

Enloe et al. (2004a) computed the power dissipation in the discharge by sampling the voltage and current waveforms across the electrodes and numerically integrating the product of the waveforms over one period of the discharge to integrate out the reactive power and account exclusively for the power dissipated in the plasma. They observed that the dissipated power also followed $V_{ac}^{3.5}$, indicating a direct proportionality with the induced velocity or momentum. They considered a model for the air above the dielectric material covering the electrode that consisted of a capacitor and resistor in series. Figure 13 shows this model for the SDBD plasma actuator. Before the air ionized, the capacitor, C_1, corresponds to the value for air. When the air ionizes, this capacitor effectively becomes a short circuit. The remaining circuit elements, R_1 and C_2 then form a voltage divider. The impedance, Z_2, of the capacitance, C_2, is given as $Z_2 = -i/\omega\ C_2$, where $\omega = 2\pi/f_{ac}$ and f_{ac} is the ac frequency. For a fixed frequency, C_2 would be a constant. Then one might expect that the electrical power dissipated by the plasma would be V_{ac}^2/R_1, or generally be proportional to V_{ac}^2. Experiments (Enloe et al. 2004a) however indicate that this is not the case.

Reasons why the power dissipated by the plasma is not proportional to V_{ac}^2 include:

1. C_2 is not constant but increases with the applied ac voltage,
2. R_1 decreases with increasing applied ac voltage,
3. both of the above.

In fact, the previous results have shown that the sweep-out velocity of the plasma front increases with increasing voltage as was illustrated in Fig. 9. Thus the area over the dielectric that makes up the capacitance, C_2, increases faster with increasing voltage. Therefore the value of C_2 is not constant but increases in proportion to V_{ac}. With regard to R_1, numerical simulations of the circuit in Fig. 13 that were intended to reproduce the output waveforms observed in experiments, indicated that the resistance needed to vary inversely with the applied voltage (Enloe et al. 2004a). Therefore both effects are in play.

The dependence of the dissipated power in the plasma and the induced momentum on the applied voltage is an important characteristic that any physical model needs to replicate. These results indicate that it must include the dynamics of the plasma initiation and sweep-out over the dielectric covered electrode that occurs twice during the ac period. An electrical model for dielectric barrier discharge by Naude et al. (2004) has addressed this with the addition of electrical elements (Zener diodes) that switch the current path between different passive circuit elements to control the characteristics with voltage and frequency.

2.2 SDBD body force models

The SDBD plasma actuator designs of the type shown in Fig. 1, have been demonstrated to induce motion in the neutral fluid that can be directly measured in terms of a reaction force on the actuator. For this to occur, there must be an electro-mechanical coupling between the moving air and the actuator. Because this coupling only occurs when the plasma is present, it can be assumed that the plasma is the intermediary. The manner that this can occur is via the electric field interactions with the charged particles in the plasma.

One of the first models for a DBD plasma actuator was developed by Massines et al. (1998a). It was a one-dimensional model based on a simultaneous solution of the continuity equations for charged and excited particles, and the Poisson equation.

Paulus et al. (1999) developed a particle-in-cell simulation to study the time-dependent evolution of the potential and the electrical field surrounding two-dimensional objects during a high voltage pulse. The numerical procedure was based on the solution of the Poisson equation on a grid in a domain containing an L-shaped electrode to the determine the movement of the particles through the grid. The simulation showed that the charged particles move towards the regions of high electric potential, creating a high electric-field strength near the electrode's edges. In addition it showed that the plasma builds up on a very short, micro-second, time scale.

A model for the body force produced by the plasma on the neutral air was presented by Roth et al. (2000). This model was based on a derivation of the forces in gaseous dielectrics given by Landau et al. (1984). In this model, the body force is proportional to the gradient of the squared electric field, namely

$$f_b = \frac{d}{dx}\left(\frac{1}{2}\varepsilon_0 E^2\right). \quad (1)$$

Enloe et al. (2004b) criticized this model because the body force does not account for the presence of the charged

particles. For example in the absence of charged particles, which might be due to the electric field being below that needed to ionize the air, the body force calculated using Eq. 1 is not zero, which is an obviously non-physical result. Boeuf and Pitchford (2005) raised the same warning in their derivation of Eq. 1.

Enloe et al. (2004b) went on to show that the body force given by Eq. 1 is only correct in the special case of a one-dimensional condition where $\vec{E} = E_x\hat{i}$ and $E_y = E_z = 0$, and $\partial/\partial y = \partial/\partial z = 0$. This special case is not relevant to the aerodynamic applications that are presented in a later section.

Another model for the body force was given by Shyy et al. (2002). A basic assumption of the Shyy et al. model was that the electric field strength, E, decreased linearly from the edge of the bare electrode towards the dielectric-covered electrode. This assumption is not consistent with the spatial illumination measurements of the discharge process made by Enloe et al. (2004b), Orlov (2006) and Orlov et al. (2006) which show an exponential spatial decay.

Suzen et al. (2005) and Suzen and Huang (2006) utilized the electrostatic model with the exponential weighting described by Orlov (2006) and Orlov et al. (2006) to compute the plasma body force using the Enloe et al. formulation (Enloe et al. 2004a, b). In their work, they proposed to split the electrostatic equations into two parts: the first one being due to the external electric field, and the second part due to the electric field created by the charged particles. Orlov (2006) suggests that this makes the problem unnecessarily complicated because it is known that the electric fields can be superimposed. This idea was used in his formulation (Orlov 2006).

Boeuf and Pitchford (2005) considered a collisional discharge in a numerical estimation of the force acting on gas molecules in a 2-D asymmetric surface DBD. For this they considered nitrogen at atmospheric pressure. They concluded that the asymmetry in the electrode configuration induces an asymmetry in the flow, comparable to a dc force in surface corona discharges.

There have been numerous models developed for DBD in air that include very complicated chemistry. These models usually include 20−30 reaction equations, each with different reaction times and energy outputs. These equations account for electron, ion-neutral, and neutral-neutral reactions in different gases that are present in the air (Gibalov and Pietsch 2000b; Golubovskii et al. 2002; Kozlov et al. 2001; Pai et al. 1996; Madani et al. 2003). For the most part, these models were developed for simple one-dimensional geometries consisting of axisymmetric facing electrodes. Recently to simplify the chemistry, Font (2004) and Font and Morgan (2005) considered the plasma discharge in a 2-D asymmetric plasma actuator that included only nitrogen and oxygen reactions. With this model, they were able to simulate the propagation of a single streamer from the bare electrode to the dielectric surface and back.

There is also a group of simplified models in which the chemical reactions are not considered, but the gas is still considered to be a mixture of ions, electrons and neutral molecules. These models were first derived for a simple one-dimensional discharge (Roy et al. 2003; Roy and Gaitonde 2004), and later extended to include two-dimensional DBD (Poggie 2005; Roy and Gaitonde 2005; Gaitonde et al. 2005b).

Likhanskii et al. (2006) modeled the weakly ionized air plasma as a four-component mixture of neutral molecules, electrons, and positive and negative ions, that included ionization and recombination processes. Their simulations indicated the importance of the presence of negative ions in the air. They also suggest that the charging of the dielectric surface by electrons in the cathode phase was critical, where they believe it acts as a "harpoon" pulling positive ions forward and accelerating the gas in the anode phase.

Generally speaking, the charged particle models can precisely describe all of the different processes involved in the plasma discharge. However they are computationally time-consuming and require significant computer resources. This is especially true if applied to air at near-atmospheric pressures. Such simulations are not suitable to be a part of a design tool that would be used in the iterative optimization of the plasma actuators, and the design of flow-control applications based on plasma actuators.

Orlov (2006) and Orlov et al. (2006) addressed the need for an efficient method for predicting the body force field of SDBD plasma actuators by developing a space-time lumped-element circuit model that is a variation of the one proposed by Enloe et al. (2004a) that was shown in Fig. 13.

A schematic of the Orlov et al. (Orlov 2006, Orlov et al. 2006) model is shown in Fig. 14. The unique aspect of this model is the division of the domain over the covered electrode into N parallel networks. The properties of each parallel network depend on its distance from the exposed electrode. These were designated parallel network 1 which is closest to the exposed electrode, to parallel network N, which extends the farthest distance over the covered electrode.

Each parallel network consists of an air capacitor, a dielectric capacitor, and a plasma resistive element as in the earlier model (Enloe et al. 2004a, Orlov 2006). Zener diodes were added to set a threshold voltage level at which the plasma initiates, and to switch into the circuit the different plasma resistance values based on the current

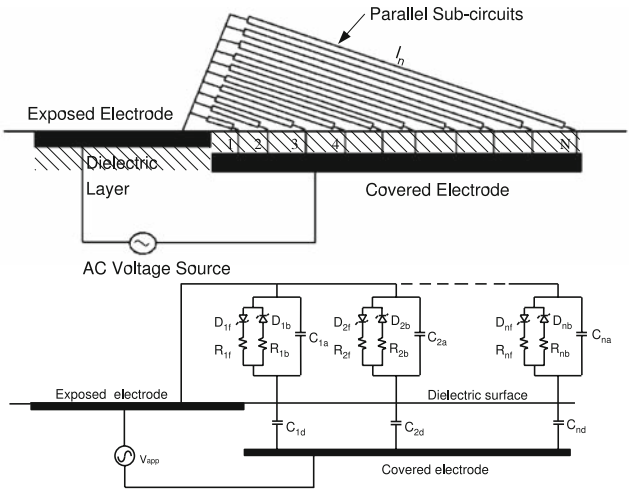

Fig. 14 Space-time lumped element circuit model for SDBD plasma actuator that divides region over covered electrode into *N* sub-regions (*left*) that each represent a parallel arrangement of circuit elements (*right*) (from Orlov 2006, Orlov et al. 2006)

direction which experiments had shown to be important. The N-circuit arrangement is shown in Fig. 14.

The value of the air capacitor in the *n*th sub-circuit is based on its distance from the edge of the exposed electrode. The resistance value in the *n*th sub-circuit is similarly based on its distance from the exposed electrode. The value of the dielectric capacitor for each sub-circuit is similar to the air capacitance except that it is based on the properties of the dielectric material.

Assuming that the paths are parallel to each other, and the length of path, l_n, is proportional to its position number, n, it then follows that the the air capacitance of the *n*th sub-circuit, C_{an}, is proportional to $1/n$, and the air resistance of the *n*th sub-circuit is proportional to n. Based on this, sub-circuits that are furthest from the edge of the electrodes have the lowest air capacitance and the largest air resistance.

For a time-varying (ac) applied voltage, the voltage on the surface of the dielectric at the *n*th parallel network is given by Eq. 2 as

$$\frac{\mathrm{d}V_n(t)}{\mathrm{d}t} = \frac{\mathrm{d}V_{\mathrm{app}}(t)}{\mathrm{d}t}\left(\frac{C_{\mathrm{an}}}{C_{\mathrm{an}} + C_{\mathrm{dn}}}\right) + k_n \frac{I_{\mathrm{pn}}(t)}{C_{\mathrm{an}} + C_{\mathrm{dn}}}, \tag{2}$$

where $I_{\mathrm{pn}}(t)$ is the time varying current through the plasma resistor. In Eq. 2, the diodes are represented by the variable k_n. When the threshold voltage is exceeded, $k_n = 1$. Otherwise $k_n = 0$.

The current through the plasma resistance, $I_{p_n(t)}$ is given by Eq. 3 as

$$I_{p_n}(t) = \frac{1}{R_n}\left[V_{\mathrm{app}}(t) - V_n(t)\right] \tag{3}$$

where $R_n = R_{nf}$ or $R_n = R_{nb}$ based on the current direction. The ratio of the two plasma resistances used by Orlov (2006) and Orlov et al. (2006) were $R_{nf}/R_{nb} = 5$, which was based on the difference in the currents measured in experiments (Orlov 2006).

The chief advantage of this formulation is that it is temporal. Therefore the effect of the ac frequency or waveform shape can be examined. The ionization dynamics such as the sweep-out velocity of the plasma can then be determined a priori.

The solution of the model equations gives the voltage on the surface of the dielectric, $V_n(t)$, and the current, $I_{p_n(t)}$, for each parallel circuit element. Figure 15 shows contours of the rectified current $\left|I_{p_n}(t)\right|$ from this space-time model for a 5 kV_{p-p}, 5 kHz sine wave that simulates the experimental conditions of Fig. 8. The current waveform is rectified to produce the equivalent of the space-time varying plasma illumination. This lumped element model reproduces many of the quantitative features of the plasma development during the ac cycle including the maximum sweep-out distance and velocity as a function of the voltage amplitude and frequency (Orlov 2006; Orlov et al. 2006). These characteristics taken from the model were plotted as a validation against the experiments in Figs. 9 and 10.

The space-time dependent voltage, $V_n(t)$, from the lumped element model is necessary to obtain the plasma body force exerted on the neutral fluid. In particular, $V_n(t)$ on the surface of the dielectric serves as the time-dependent

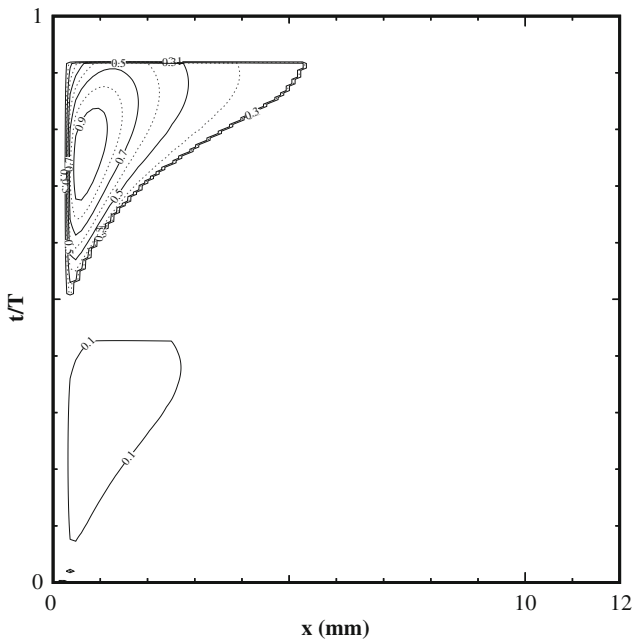

Fig. 15 Space-time variation of rectified current obtained from lumped circuit model for SDBD plasma actuator corresponding to one period, *T*, of the input AC cycle. (from Orlov 2006, Orlov et al. 2006)

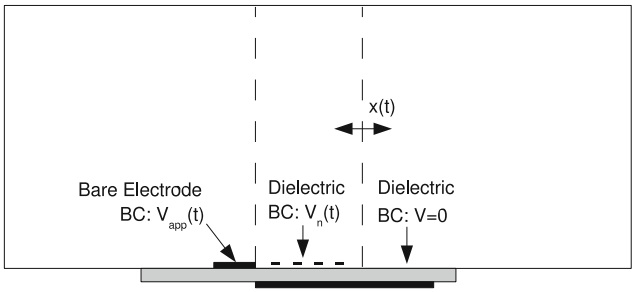

Fig. 16 Computational domain for calculation of unsteady plasma body force

boundary condition for the electric potential, φ, found in the solution of the electrostatic equation

$$\nabla(\varepsilon\nabla\varphi) = \frac{1}{\lambda_D^2}\varphi. \tag{4}$$

The time-dependent extent of the plasma on the surface of the dielectric, $x(t)$, specifies the region of the presence of charges above the covered electrode. This defines a moving boundary as shown in Fig. 16. The boundary value of the electric potential on the bare electrode is the applied voltage $V_{app}(t)$. At the outer boundaries at "infinity", the boundary conditions are $\varphi = 0$.

The electric potential, $\varphi(t)$, is determined at small time steps of the ac cycle. This is then used to calculate the time-dependent body force produced by the plasma, given by

$$\vec{f}_b(t) = \rho_c\vec{E}(t) = -\left(\frac{\varepsilon_0}{\lambda_D^2}\right)\varphi(t)\vec{E}(t). \tag{5}$$

As a result of the ac input to the actuator, the body force is periodic. This has been evident by a common observation of an acoustic "tone" related to the ac frequency of the plasma actuator when operating (Enloe et al. 2004a; Porter et al. 2006). Figure 17 shows the computed space variation of the normalized body force magnitude, $|f_b|/|f_{bmax}|$, and the corresponding vectors at two instants in the ac cycle that were obtained from the Orlov (2006), Orlov et al. (2006) model. The time instants are indicated by the dots over the ac waveform. These are in the center of the blue bands where the air is ionized as discussed with reference to Fig. 7. The region a–b is where electrons efficiently move from the bare electrode to the dielectric. The region c–d is where the electrons move from the dielectric to the bare electrode which is less efficient. For the former, body force magnitude extends further over the region of the covered electrode. For the latter, the extent is less. Both these are consistent with the distribution of the light emission during the ac cycle.

One observes that the largest magnitude of the plasma body force is near the edge of the bare electrode closest to the covered electrode, $x = 0$. From that location, the magnitude decays rapidly over the surface of the dielectric. A curve fit of the spatial decay by Orlov (2006) indicated that it was exponential.

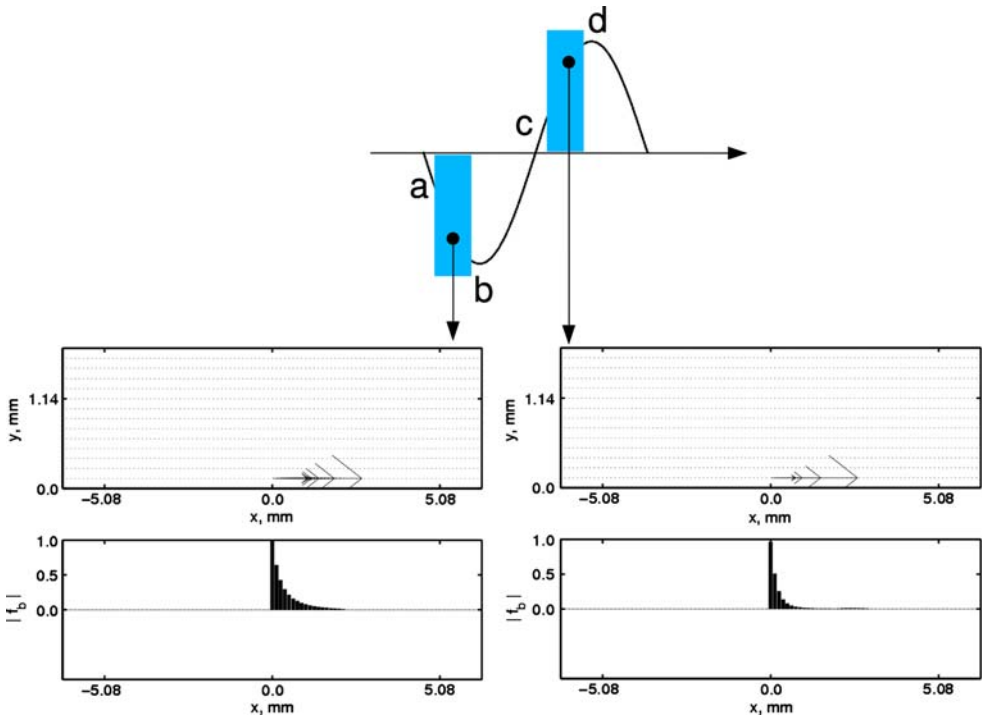

Fig. 17 Body force magnitude and vector at two points in the ac cycle for generic asymmetric electrode configuration like that in Fig. 1. (from Orlov 2006, Orlov et al. 2006)

In the Orlov (2006), Orlov et al. (2006) model the values of the lumped circuit elements are only a function of the electrode geometry. There are experiments ongoing that are investigating how these might change with different conditions including pressure and gas composition. There is no evidence that incompressible flow speeds ($0 \leq M \leq 0.5$) modify the behavior of the actuator effect. Compressibility effects are an open question.

A frequently discussed topic is the vector direction of the plasma body force during the ac cycle. The formulation given in Eq. 5 indicates that throughout the ac cycle, the body force is always oriented in the direction from the bare electrode towards the covered electrode. This could be the result of the assumptions made in the formulation of the model, in particular the "quasi-steady" assumption that the time scale of the electron and ion movement is much smaller than the ac period.

This is certainly true for the electrons. The question is whether it is true for the ions. The charged particle simulations of Font (2004) and Font and Morgan (2005) that included nitrogen and oxygen reactions, followed the propagation of a single streamer from the bare electrode to the dielectric surface and back. They suggested that during the "forward discharge" when the electrons are pushed away from the bare electrode and the positive ions are pulled back towards the bare electrode, the net momentum is not zero, but favors the ions so that there is a net momentum towards the bare electrode. In the "back discharge" when the electric field is reversed, the Font et al. simulations have a resultant force that is away from the bare electrode, towards the dielectric (as in the Orlov 2006; Orlov et al. 2006 model). The magnitude of body force in the "back discharge" was significantly larger than in the "forward discharge" so that the cycle-averaged vector from the simulation was overwhelmingly towards the dielectric, as observed in the time-averaged experiments (Iqbal et al. 2007).

This scenario of Font (2004) and Font and Morgan (2005) might be categorized as "PUSH-pull" where the upper or lower case signifies the relative magnitude. The Orlov (2006) and Orlov et al. (2006) model would indicate "PUSH-push". What is the experimental evidence?

Forte et al. (2006) performed time resolved LDV measurements of the flow induced by an SDBD plasma actuator similar to Fig. 1, in a quiescent neutral flow. With this, they were able to capture the streamwise and wall-normal velocity components within a period of the AC input. Of particular interest to this discussion is the streamwise (u) velocity component. The LDV measurements indicated that during the ac cycle the u-component oscillated between a large-positive u and a small but positive u, and was never negative. This result supports a "PUSH-push" scenario. Recent experiments by Enloe et al. (Porter et al. 2007) indicate a "PUSH-push" scenario, although the magnitude of the smaller push may be somewhat less than predicted by the Orlov (2006) and Orlov et al. (2006) model.

2.3 Optimization

The insight that comes from developing a better understanding of the physics behind the SDBD plasma actuator can suggest approaches to optimize its performance. For example, the observations that the ionization occurs as long as the difference between the instantaneous ac potential and the charge buildup on the dielectric exceed a threshold value suggest that there are ac waveforms that are optimal. For example, a square wave is least optimum, a sine wave is better, and a triangle wave is better yet. This can be extended further by considering a waveform that emphasizes the time given to the "PUSH" and minimizes the time of the "push". This waveform is a sawtooth whereby the sloping part should correspond to when the potential is such that the electrons are being deposited onto the dielectric. Enloe et al. (2004a) verified this experimentally.

As was shown in Fig. 11, the surface area of the dielectric over the covered electrode is a factor in the maximum body force. In contrast to this, the area of the exposed electrode is not a factor. However, the thickness, or rather sharpness of the electrode edge facing the covered electrode, strongly affects the body force. This was demonstrated in experiments by Enloe et al. (2004b) who compared bare electrodes consisting of flat copper tape of different thicknesses (0.08–0.64 mm), or metal music wire of different diameters (0.36–0.98 mm), on the induced thrust produced by the actuator. In general, the thrust per unit power was larger when the thickness or diameter of the bare electrode was smaller (sharper). The reason for this is that the sharper edge concentrates electric field lines which locally increases the electric field, and thereby the body force.

Forte et al. (2006) experimentally examined the effect of the amount of overlap between the bare and covered electrodes in an asymmetric arrangement like that in Fig. 1. They defined the gap spacing, g, to be positive when there was a non-overlaping distance between the edges. Interpreting their results, and normalizing the gap by the width of the covered electrode L_{ce}, which must be a factor, they found that there was little effect on the maximum induced velocities for $0 \leq g/L_{ce} \leq 2$. For larger (positive) gaps or overlap, the effectiveness of the plasma actuator dropped off rapidly.

Forte et al. (2006) also investigated multiple actuators in series. For their maximum number of four actuators, they found a constant increase in velocity past each actuator. This was consistent with the results of Post (2004) and

Corke et al. (2007a) as well as the underlying physics that the effect of the plasma actuator on the neutral flow is that of a body force, which is additive. Forte et al. investigated only one configuration of series actuators. One can expect that there is an optimum spacing that scales with the length of the covered electrode, L_{ce}, and dielectric material thickness. This has been investigated by Iqbal et al. (2007).

Orlov (2006) and Orlov et al. (2006) examined the effect of the ac frequency and dielectric material properties on the plasma body force and heat generated by the plasma. An example is shown in Fig. 18. This is based on simulations using the SDBD model discussed in the previous section. The bottom plot shows the effect of the ac frequency on the body force for dielectric layers with three different dielectric coefficients, ε. The top plot shows the power dissipated by the plasma for one of the dielectric coefficients, $\varepsilon = 100$.

The simulations indicate that for a given SDBD design, there is an optimum frequency at which the body force magnitude is a maximum. In contrast, the dissipated power increases monotonically as the ac frequency increases. This indicates that the optimum performance of the actuator requires the proper selection of the driving ac frequency. If the frequency is too low, the body force will be low. If the ac frequency is too high, past the optimum, the power that would nominally go into producing the body force will instead go into heating the air.

The optimum frequency of the plasma actuator depends on the dielectric properties of the material, or more specifically on the bulk capacitance of the actuator. The capacitance is proportional to ε/h, where h is the thickness of the dielectric. In the example, only the dielectric coefficient was changed to change its capacitance. It could have been changed through the thickness of the dielectric or in combination with ε. For the large range of values examined, the optimum ac frequency to achieve the maximum body force changed from approximately 10–1,000 Hz. For Kapton with $\varepsilon = 3.3$, and the typical thicknesses of 0.15 mm, the optimum ac frequency is in the range of 5 kHz.

There are two important properties of the dielectric material: the breakdown voltage per thickness (volts/mm), and the dielectric coefficient, ε. The minimum thickness of the dielectric needs to be sufficient to not break down at the applied voltage. Although for some materials, this can be accomplished with only a fraction of a milimeter of thickness (0.05 mm typical for Kapton). Recent evidence (Iqbal et al. 2007) shows a benefit in using thicker dielectric layers made of materials that have lower dielectric coefficients. Figure 19 shows the thrust measured with different dielectric materials having different thicknesses from Iqbal et al. (2007). The thrust was measured as previously shown in Fig. 12. In each case in Fig. 19, except for the 12.70 mm thick Teflon, the point with the highest induced thrust corresponded to the power limit of the actuator power supply. For the 12.70 mm thick Teflon, the highest thrust corresponded to the maximum voltage that could be produced by the power supply.

In general, the thicker material caused the threshold voltage needed to ionize the air to increase. Thus the voltage required to produce the same thrust increased with increasing material thickness.

The SDBD plasma actuators are voltage driven devices, with the thrust being proportional to the voltage to the 3.5 power as was shown in Fig. 12. When the actuators reached their thrust limits, it was because the current

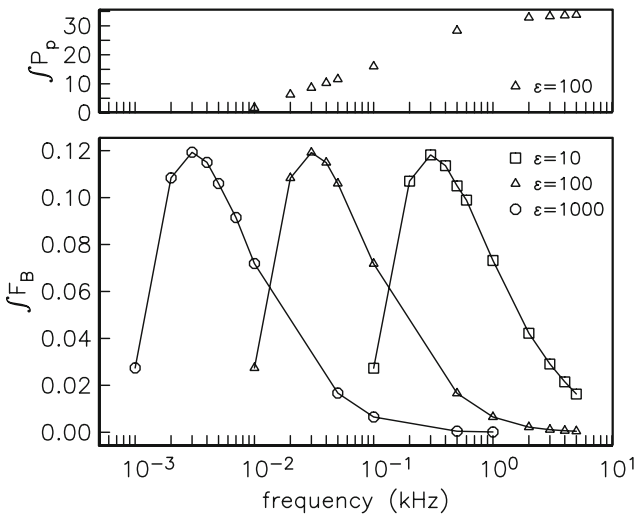

Fig. 18 Effect of dielectric properties on body force (*bottom*) and power dissipated (*top*) for a SDBD plasma actuator. (from Orlov et al. 2006, Orlov et al. 2006)

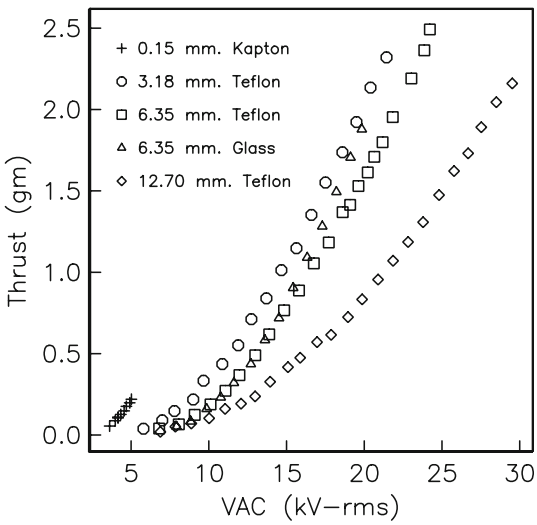

Fig. 19 Induced thrust from SDBD plasma actuator for different dielectric thickness and materials. (from Iqbal et al. 2007)

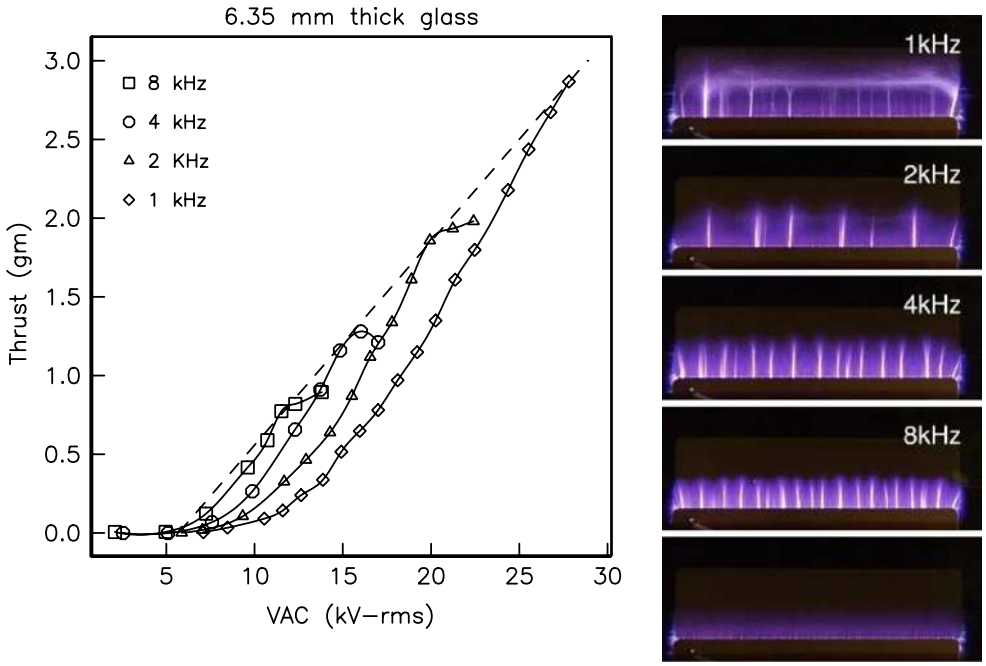

Fig. 20 Induced thrust from SDBD plasma actuator for 6.35 mm thick glass dielectric for different frequencies (*left*) and corresponding images of plasma for each frequency at maximum thrust (*right*). From Iqbal et al. (2007)

became too large, which prevented any further increase in voltage at the fixed maximum supply power. Comparing the Teflon dielectric material, the thicker material resulted in larger maximum thrust (the 12.70 mm Teflon would have exceed the others had the voltage been higher). For the same thickness (6.35 mm) of Teflon and glass, the Teflon could achieve a larger voltage (at fixed power) and therefore had a higher maximum thrust. The difference between these two was the dielectric coefficients, $\varepsilon = 2.0$ for Teflon and $\varepsilon = 3.8$ for glass. Therefore for the same thickness, the capacitance of the Teflon actuator was almost half that of the glass actuator. Note these were operated with ac frequencies that were different and optimized for maximum thrust (Orlov 2006; Orlov et al. 2006). The dielectric coefficient for Kapton is 3.3. This coupled with the small thickness made its capacitance approximately 70 times that of the 6.35 mm thick Teflon actuator. The impact is that its maximum thrust is approximately 10 times less than the Teflon actuator! Almost all of the past SDBD plasma actuator flow control was performed with a thin Kapton dielectric material (Corke et al. 2002, 2004, 2006b; Nelson et al. 2006a; Patel et al. 2006; Huang 2005; Huang et al. 2006a, 2006b; List et al. 2003; Suzen et al. 2007; Rizzetta and Visbal 2007; Rivir 2007; Post and Corke 2003, 2004, Post 2004). Although these were successful in their applications, the flow control potential is considerably better with these more optimized actuator designs.

As pointed out by Orlov (2006) and Orlov et al. (2006), the choice of the driving ac frequency is critical to attaining the maximum body force. This was investigated by Iqbal et al. (2007) using a 6.35 mm thick glass dielectric actuator. The results are shown in Fig. 20. The plot on the left side of the figure shows thrust produced by the SDBD plasma actuator as a function of the applied ac voltage. The different cases correspond to different ac frequencies of the applied voltage. The images on the right side of the figure show the ionized air. The lower image is representative of the uniform ionization that occurs within the voltage range where the thrust is proportional to voltage to the 3.5 power. The other four images correspond to the maximum thrust point at the respective ac frequencies in the plot on the left. For this actuator design, the 8 kHz ac frequency has the lowest maximum thrust and the 1 kHz has the highest thrust. Again at fixed power ($i \times V$), if the current (i) is too large, the applied voltage (V) will decrease and the body force (thrust) will decrease. The visible indication of the increased current is the appearance of the bright filaments in the plasma. The spacing between filaments appears to be somewhat uniform and proportional to the inverse of the ac frequency. As mentioned in Sect. 1, Kline et al. (2001) observed distinct filament patterns that sometimes were regular. It is interesting to note that the voltage where these first occurred varied linearly with frequency. This is indicated by the dashed line in the plot and signifies that $T_{\max} \propto f^{-1}{}_{\mathrm{ac}}$.

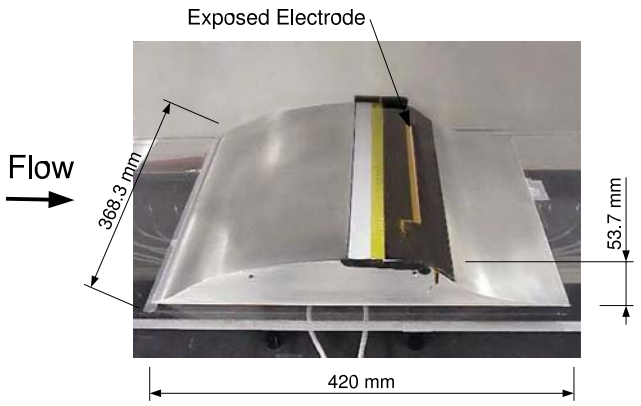

Fig. 21 Photograph of hump model used for the study of turbulent boundary layer separation control using SDBD plasma actuators (from He 2008; He et al. 2007)

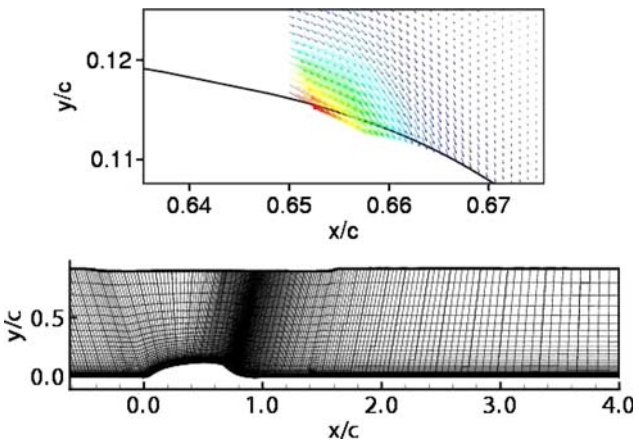

Fig. 22 Time-averaged plasma actuator body force vector distribution used in flow separation control simulation (*top*) and computational grid (*bottom*) used in numerical flow solver that includes body force. (from He 2008)

The SDBD plasma actuator power systems used for the thick dielectric experiments by Iqbal et al. (2007) were designed to develop large ac voltages at the optimum frequencies, which tended to be lower than with the thin Kapton film actuator design. They consisted of a low power function generator, signal amplifier and a step-up transformer. The signal amplifier needed to have sufficient power to drive the transformer. The transformer was the most critical element since it needed to be designed with a high enough winding ratio to reach the desired voltage, and to operate efficiently at the relatively low (order 1–2 kHz) frequencies that were optimum for the thick dielectric actuators. These transformers were custom made for this application by Corona Magnetics, Inc.[1]

3 Example applications

3.1 Turbulent boundary layer separation control

The effect of the plasma actuator is incorporated into numerical flow solvers by adding the actuator body force into the momentum equation. Numerically, this is a particularly efficient approach because the body force is not coupled to the flow parameters and therefore can be calculated off-line for the particular geometry. As an example, the steps associated with this are presented for a geometry consisting of a wall-mounted hump that was used in a 2004 NASA Langley CFD validation workshop on canonical turbulent separated flows. The hump has a relatively long fore-body and an aft portion with a short concave ramp where flow separation occurs. Experimental data for this geometry are well documented (Greenblatt et al. 2004). Figure 21 shows a photograph of the hump model used in the experiments of He (2008) and He et al. (2007). The exposed electrode of a spanwise plasma actuator is noted in the photograph. The location was at $x/c = 0.66$ (c = total length of the model = 420 mm), which was just upstream of where the boundary layer flow separated.

The Orlov (2006) SDBD model described in the previous section was used to calculate the body force vectors produced by the actuator. In order to replicate the experiment, the electrodes were 1/2 inch wide, and the dielectric material was a 0.006 inch thick Kapton. The ac-cycle-averaged body force vectors are shown in the top part of Fig. 22.

The body force effect of the plasma actuator has been included in a number of flow solvers including NASA's CFL-3D (Corke et al. 2006a), FLUENT (Orlov 2006; Orlov et al. 2006), and WIND-3D (Nelson et al. 2006b), as well as other general Navier–Stokes codes (Gaitonde et al. 2005a; Suzen et al. 2005; Suzen and Huang 2006; Rizzetta and Visbal 2007). The flow simulations for the hump model were performed by He (2008) using FLUENT. This utilized a segregated solver to solve the two dimensional Reynolds-averaged Navier–Stokes equations with a user-defined module for adding the body force distribution to account for the plasma actuator effect. The computation was done on a 412 × 46 ($x \times y$) grid. The computational grid used by He is shown in the bottom part of Fig. 22.

A comparison between the experiment and simulation of the pressure coefficient distribution on surface of the hump model is shown in Fig. 23. The base flow with the plasma actuator off is shown as the circle symbols for the experiment, and as the solid-thick curve for the simulation. He (2008) and He et al. (2007) investigated a number of different turbulence models and found that a k-ε model had the best agreement with his and other published (Greenblatt

[1] 201 Corporate Terrace, Corona, CA.

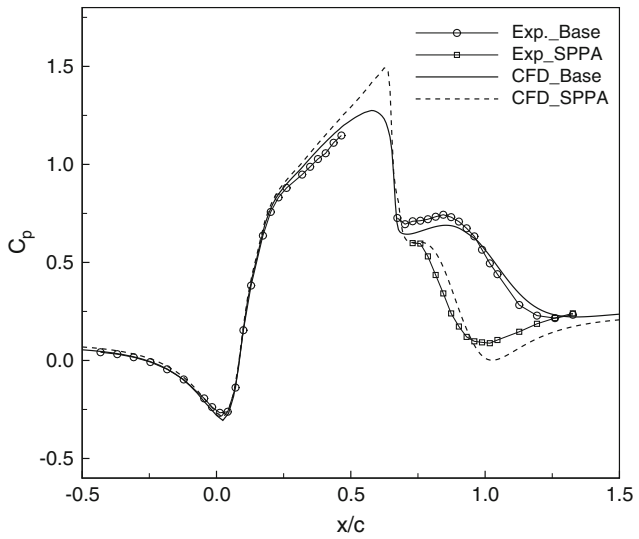

Fig. 23 Comparison between the surface pressure pressure distribution over the hump model of the experiments and simulations with and without the plasma actuator operating. (from He 2008; He et al. 2007)

et al. 2004) experimental data. This was the turbulence model used with both the base-flow and plasma actuator flow simulations.

For the base flow, the up-turn in the pressure distribution at $x/c = 0.66$ is indicative of the flow separation. Reattachment occurs where the pressure distribution becomes flat near $x/c = 1.25$. The flow separation causes a flow recirculation region that is evident it the streamline pattern from the simulation results shown in Fig. 24a.

The C_p distribution with the square symbols in Fig. 23 shows the experimental results with the plasma actuator operating. This indicates that there is a good degree of pressure recovery, and an upstream movement of the reattachment location to approximately $x/c = 1$. The results from the simulation are shown as the dashed curve. The agreement is relatively good. The streamline pattern from the simulations with the plasma actuator operating, that correspond to this C_p distribution, is shown in Fig. 24b. These show a clear reduction on the size and extent of the recirculation zone. These results were for "steady" operation of the plasma actuator. He (2008) has examined so-called "unsteady" operation in which the plasma actuator is periodically turned on and off at a frequency that is much lower than the ac frequency used to ionize the air. The choice of the unsteady frequency is based on the extent of the separation bubble and free-stream speed. He (2008) for airfoil leading-edge separation, and Huang et al. (2006b) for laminar boundary layer separation verified that there was an optimum frequency corresponding to a dimensionless frequency, $F^+ = fL_{sep}/U_o = 1$, that would produce the maximum pressure recovery. In the dimensionless frequency, L_{sep} is the length of the flow separation region, and U_o is the local outer mean velocity.

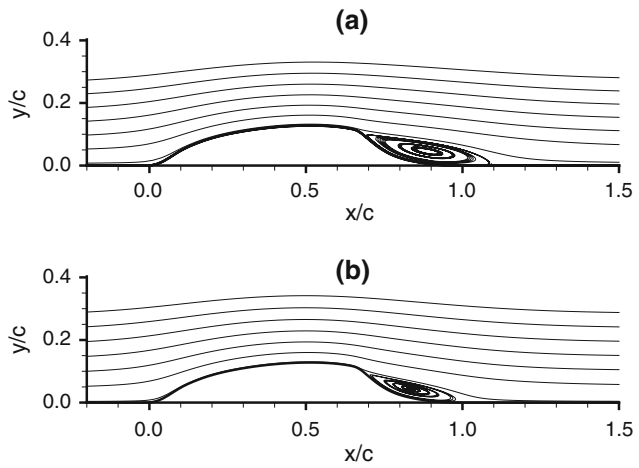

Fig. 24 Streamline patterns for flow over hump models from numerical simulations of the (a) base flow and (b) with SDBD plasma actuator located at $x/c = 0.66$. (from He 2008; He et al. 2007)

For the hump model, He (2008) has also investigated plasma actuators with electrodes oriented in the streamwise direction. These were designed to act as delta-tab streamwise vortex generators. They were found to reduce the separation region similar to the spanwise-oriented plasma actuator, and the flow simulations with and without the plasma actuator operating were found to agree well with the experiment.

3.2 Steady airfoil leading-edge separation control

Plasma actuators have been used extensively to control leading-edge separation at high angles of attack (Post 2004; Post and Corke 2003; Corke et al. 2004; Goeksel et al. 2006; Goeksel and Rechenberg 2004). This has been demonstrated on a number of 2-D airfoil shapes including NACA 0009, 0012, 0021, 66_3-018, and a HS3412, as well as highly swept 3-D wing models such as the NASA 1303 planform (Patel et al. 2007a, b, 2008). The chord Reynolds numbers in these experiments ranged from 0.077×10^6 to 1.4×10^6, and encompassed free-stream speeds from 10 to 90 m/s.

The approach has been to locate an actuator directly on the leading edge, whereby the body force induces a flow towards the suction side of an airfoil. This is illustrated in the left part of Fig. 25 for a NACA 0015 airfoil. The dielectric layer in this case is Kapton film. The right part of the figure shows the averaged body force vectors computed from the SDBD actuator model.

An example of leading-edge separation control is shown in Fig. 26. This shows the lift coefficient versus angle of attack with the plasma actuator off and on in "steady"

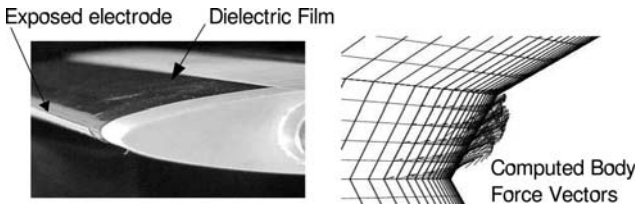

Fig. 25 Photograph of NACA 0015 airfoil model with the plasma actuator applied onto the surface of the airfoil at the leading edge (*left*) and the computed body force vectors produced by actuator (*right*) [from He (Corke et al. 2004)]

operation. The measurements, obtained using a force balance, correspond to the symbols. The curves correspond to numerical flow simulations using a modified version of CFL3D (Voikov et al. 2004) that incorporated the actuator body force effect.

With the actuator off, the lift increases linearly up to the stall angle, which is approximately $\alpha = 14°$. The solid curve is the numerical prediction without the actuator. Stall corresponds to full leading-edge separation, with a separation bubble that covers the total suction surface of the airfoil. This is documented in the top photograph in the right part of Fig. 26, which shows smoke streaklines over the airfoil at a post-stall, $\alpha = 16°$.

When the actuator is on in "steady" operation, the bottom flow visualization photograph shows the flow to be attached at $\alpha = 16°$. Lift measurements indicated that the stall angle increased to 18°. This agreed well with the numerical flow simulation (dashed curve) from Voikov et al. (2004).

The effect of the actuator on separation prevention is enhanced when the actuator is impulsively cycled on and off at a frequency, f, corresponding to $F^+ = fc/U_o = 1$, where c is the airfoil chord length. This is demonstrated in Fig. 27 which compares the lift versus angle of attack between the steady and unsteady plasma actuator conditions.

The unsteady actuator at $F^+ = 1$ substantially increased $C_{L_{max}}$ and α_{stall}, and maintained lift to $\alpha = 22°$, which was 7° past the natural stall angle of attack, and 4° past that of the steady actuator operation. The numerical simulations of the unsteady actuator (Voikov et al. 2004) agreed well with the experiments. In this case the effect of the unsteady actuation was included by turning the body force on and off at a specified interval in the computational time steps that corresponded to the F^+ used in the experiment.

3.3 Oscillating airfoils dynamic stall control

The same NACA 0015 section shape was used by Post (2004) to investigate the control of dynamic stall on an oscillating airfoil. The application was helicopter rotors. In that study, the airfoil went through a periodic pitching cycle with an angle of attack given by $\alpha(t) = \alpha_{mean} + \alpha_{amp}\sin(\omega t)$. Post examined a range of combinations of mean angle of attacks and pitch angle amplitudes. An example of these are shown in Figs. 28, 29, 30, which correspond to $\alpha_{mean} = 10°$ and $\alpha_{amp} = 5°$. The oscillation frequency expressed as a reduced frequency, $k = \omega c/2U_\infty$, was 0.08. Flow with $k > 0.05$ is considered unsteady. In a typical helicopter, $0.07 \leq k \leq 0.15$.

The airfoil was oscillated about its quarter chord location. The motion was driven by a programmable servo motor. Two output encoder signals provided feedback on the instantaneous angle of attack during the pitching cycle. The airfoil was instrumented with an array of surface pressure ports that were used to determine the static pressure distribution, and integrated to obtain the lift during the pitching cycle. Flow visualization similar to that used to

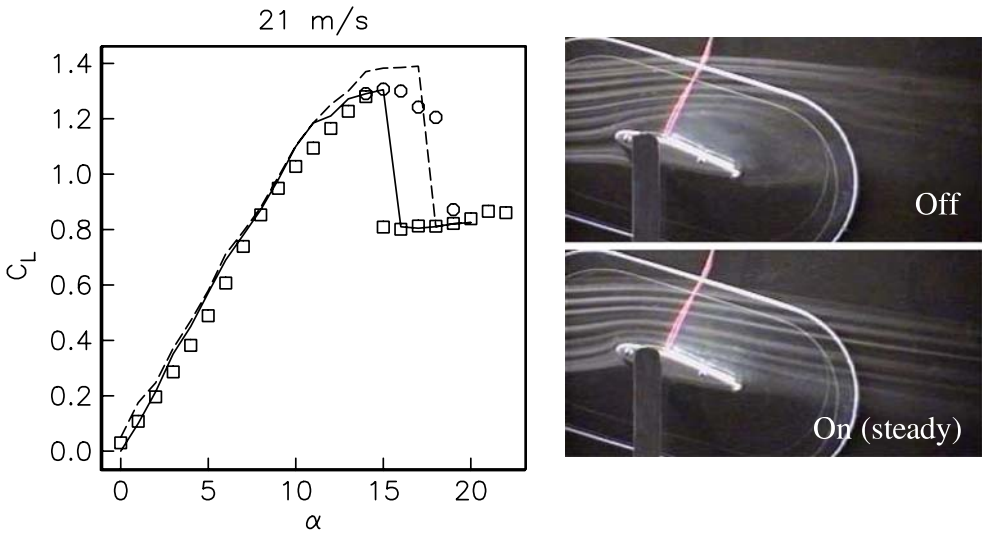

Fig. 26 Lift coefficient versus angle of attack for NACA 0015 airfoil with leading-edge actuator off and on (steady) from Corke et al. (2004), and corresponding visualized flow at $\alpha = 16°$; from Post (2004). Curves are from numerical simulations by Voikov et al. (2004). $Re_c = 0.217 \times 10^6$

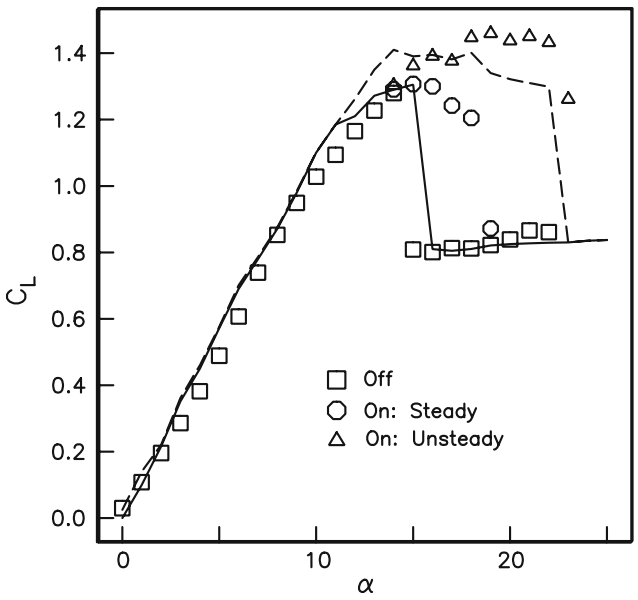

Fig. 27 Lift coefficient versus angle of attack with leading-edge actuator off and on at optimum unsteady frequency, from Corke et al. (2004). Curves are from numerical simulations by Voikov et al. (2004). $Re_c = 0.217 \times 10^6$. Example of time series used as input to actuator for unsteady operation shown at the *left*

produce the flow images in Fig. 26 was used to record the flow field at different angles of attack in the pitching cycle. These are shown for the baseline (no flow control) condition in Fig. 28.

The image in the top left of Fig. 28 at $\alpha = 5°$ corresponds to the beginning of the periodic cycle. The subsequent images record the flow as the airfoil pitches to higher angles of attack, reaching the maximum angle of 15°. The airfoil then proceeds to pitch down in the cycle until it reaches its minimum at $\alpha = 5°$, where the cycle repeats. During pitch-up, the flow appears to remain attached. During pitch-down, the flow appears to initially separate at the maximum thickness point and progress forward towards the leading edge. It only appears to fully re-attach at the start of the pitch-up portion of the cycle beginning at $\alpha = 5°$.

Figure 29 shows flow visualization records for the same conditions of Fig. 28 except with the addition of a SDBD plasma actuator at the leading edge. The plasma actuator configuration was identical to that used in the fixed angle of attack example illustrated in Fig. 25. The plasma actuator operated continually throughout the pitching cycle. Examining the images in this case, one observes that the flow remains attached throughout the cycle.

The impact of the flow control on the pitching airfoil can be quantified by the effect on the lift force. This is documented in Fig. 30 which shows the lift coefficient during pitching cycle for the cases without and with the plasma actuator operating. In each case, the C_l versus α cycle loops in the clockwise direction. The interior of the loop for the baseline case is larger owing to the flow separation (dynamic stall) on the pitch-down portion, causing a loss of lift. The plasma actuator maintains an attached flow over the whole cycle. This has the effect of closing the loop and achieving virtually linear lift versus angle of attack behavior in pitch-up and pitch-down that is associated with

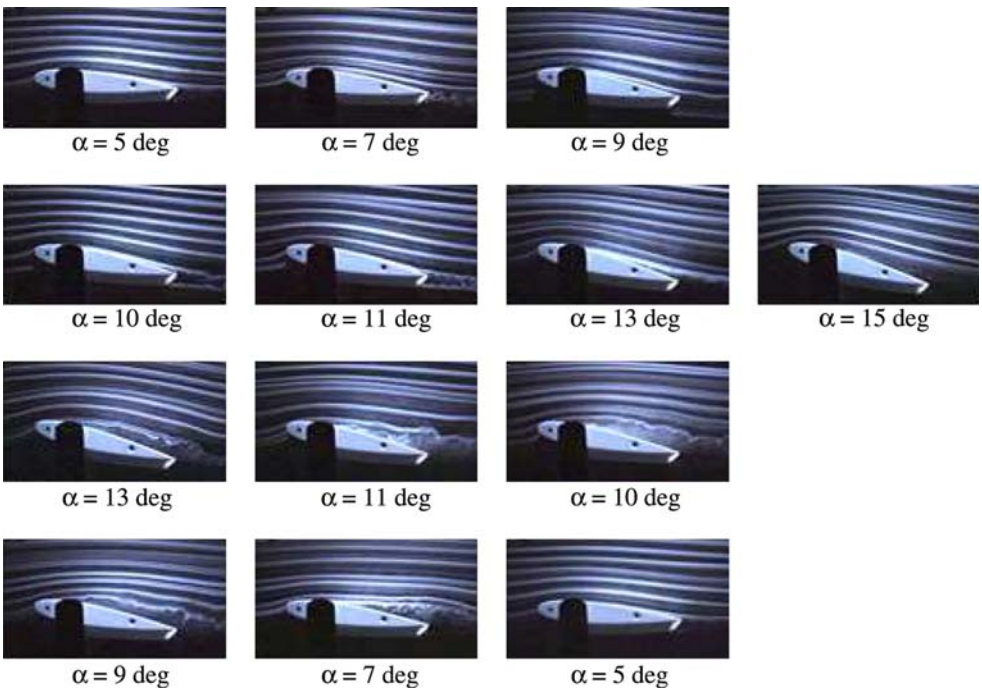

Fig. 28 Visualization of the base flow over a periodic pitching NACA 0015 airfoil captured at different angles of attack in the cycle. (from Post 2004)

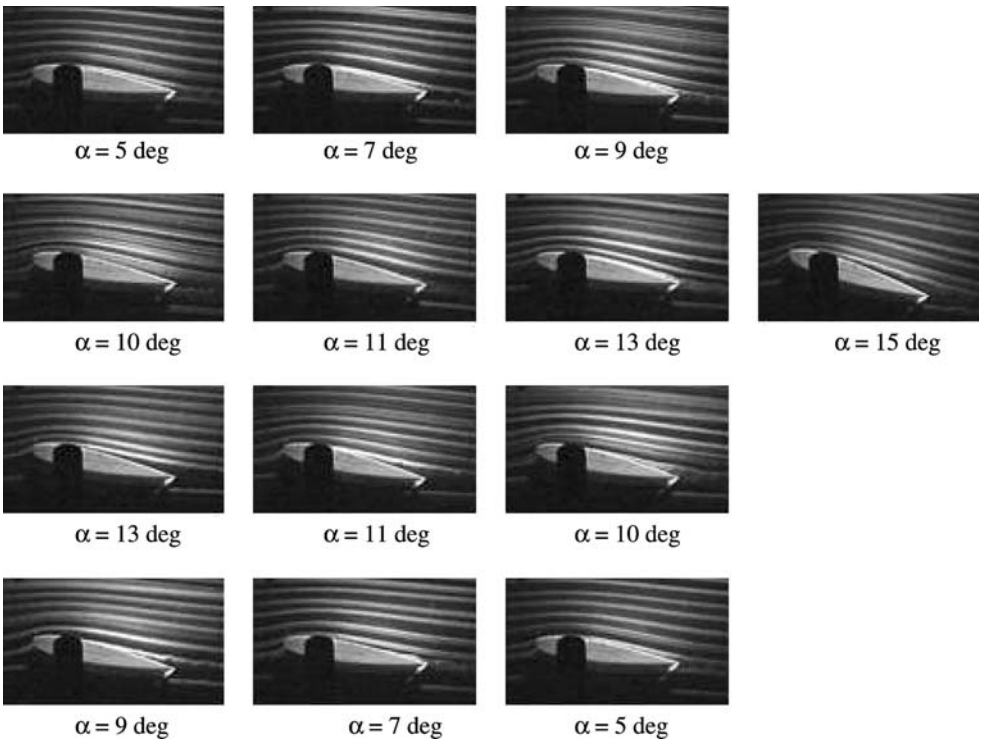

Fig. 29 Visualization of the flow over a periodic pitching NACA 0015 airfoil captured at different angles of attack in the cycle with a leading-edge plasma actuator. From Post (2004)

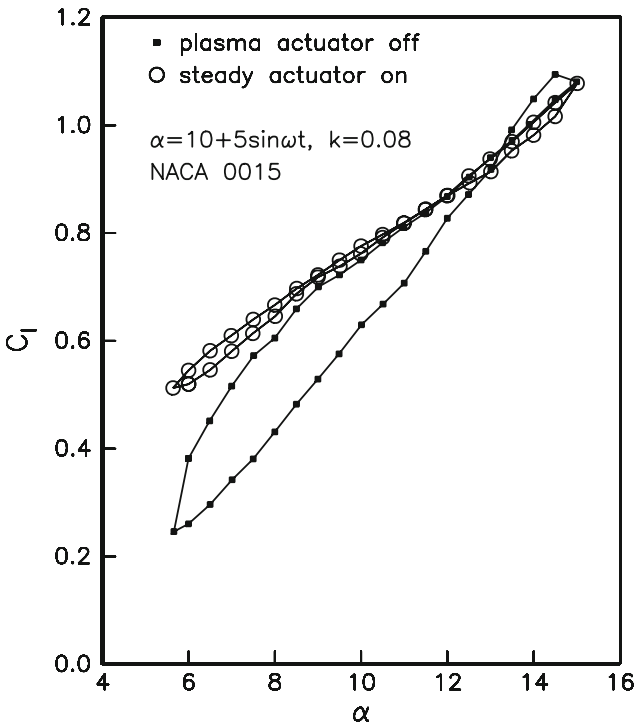

Fig. 30 Lift coefficient versus angle of attack for a periodic pitching NACA 0015 airfoil with a leading-edge plasma actuator off and on corresponding to the flow visualization in Figs. 28 and 29, respectively. (from Post 2004)

a steady airfoil. The improvement in the cycle-integrated lift in this case was approximately 30%. Post (2004) has demonstrated similar improvement in the lift for a range of oscillating airfoil conditions using steady and unsteady plasma actuator operation.

3.4 Circular cylinder wake control

Thomas et al. (2008) applied SDBD plasma actuators on a circular cylinder to suppress the VonKarman vortex street. The application is to lower the acoustic levels originating from the main landing gear strut of commercial aircraft. A schematic of the plasma actuator arrangement used on the cylinder is shown in the left part of Fig. 31. The cylinder was made from a 7.62 cm diameter hollow glass tube. The wall thickness of the glass cylinder, which served as the dielectric, was 6.35 mm. A similar thickness glass dielectric was one of the cases examined in the thrust experiments presented in Figs. 19 and 20.

Four plasma actuators were used. These were located on the downstream half of the cylinder starting at 90°, 135°, 225° and 270° as measured in the clockwise direction from the stagnation line on the upstream side of the cylinder. The plasma actuator locations were defined to be at the downstream edge of the exposed electrodes. The actuators were like the asymmetric electrode design shown in Fig. 1. The dielectric between the electrodes was the glass wall of the cylinder. The pairs of electrodes at 90° and 270°, and 135° and 225° could be operated separately.

The right part of Fig. 31 shows the visualized flow around the cylinder at $Re_D = 30{,}000$. The flow visualization used a vertical array of smoke streaklines that were

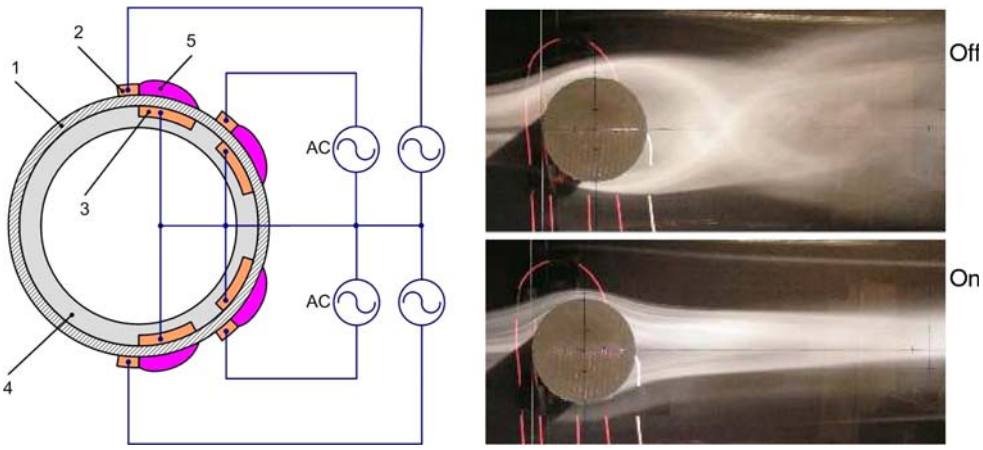

Fig. 31 Arrangement of SDBD plasma actuators for suppressing the VonKarman vortex street behind a circular cylinder (*left*) (*1*. Glass wall dielectric, *2*. Exposed electrodes, *3*. Covered electrodes, *4*. Insulation, *5*. Ionized air.) and visualization images of the base flow around a circular cylinder at $Re_D = 30{,}000$ (*right-top*), and with plasma actuators operating (*right-bottom*). (from Thomas et al. 2008)

introduced upstream of the contraction of the open-return wind tunnel. The top photograph corresponds to the base flow with the plasma actuators off. The camera time-averaged the image, however traces of the alternate vortex shedding are evident, along with an indication of the overall wake width. The bottom photograph corresponds to when all four plasma actuators were operating. In this case the vortex shedding had been completely suppressed. Thomas et al. (2008) has investigated steady and unsteady plasma actuator conditions. The bottom photograph corresponds to a steady actuator condition. As with other separated flows (Corke et al. 2004; Huang et al. 2006b), Thomas et al. observed an optimum unsteady frequency at $F^+ = 1$, where the separation length used in scaling the unsteady frequency was the cylinder diameter.

Matlis and Corke (2008b) have applied the same approach to controlling the wake on a cylinder in a Mach 1.4 free-stream. The Schlieren photograph of the flow around the cylinder is shown in left part of Fig. 32. The cylinder consisted of a ceramic tube with two internal passages that were equally spaced from the outside radius of the cylinder. The cylinder was oriented so that the internal holes were aligned in the vertical direction and perpendicular to the flow direction. Wires ran through the internal passages to form the covered electrodes of a pair of plasma actuators. The wall of the ceramic cylinder acted as the dielectric material. Ceramic is an excellent dielectric material, and also one of those represented in Fig. 19. Two narrow strips of 0.025 mm thick copper tape were affixed to the outside of the cylinder, spanning the length of the cylinder. These acted as the exposed electrodes. The downstream edges of the copper strips were located at $\pm 90°$ from the upstream stagnation line on the cylinder. The cylinder was held in the stream by two posts. The posts were 7.62 cm apart. The test section inside dimensions were 10.2 by 12.7 cm. The Schlieren photograph shows the shock pattern coming off of the cylinder and reflected shocks from the tunnel ceiling and floor.

A photograph of the plasma (blue) with the actuator operating in the Mach 1.4 flow is shown in the bottom-right

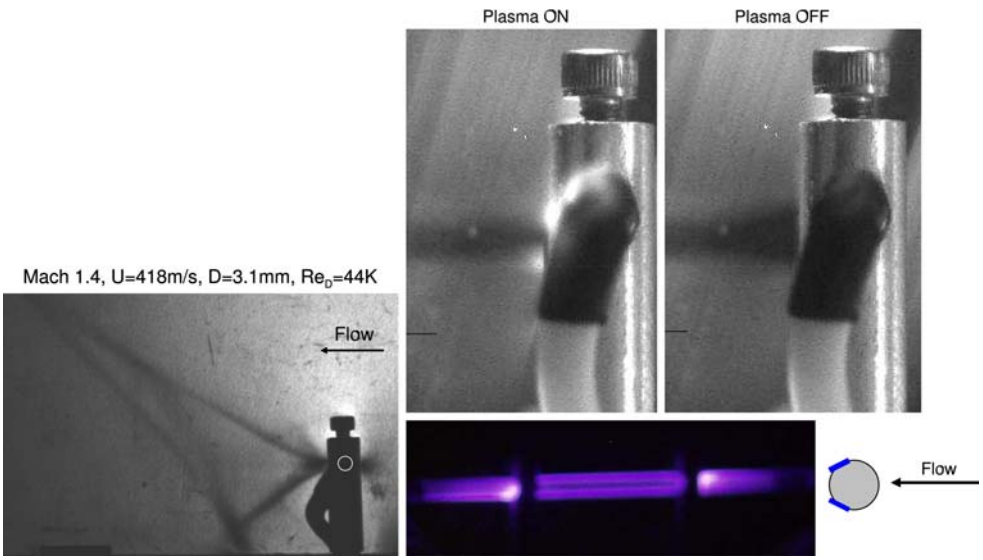

Fig. 32 Schlieren photograph of the flow around a 3.1 mm. diameter circular cylinder in a Mach 1.4 free-stream (*left*), and photographs of the visualized near wake region of the cylinder with plasma actuators off and on (*right*). $Re_D = 44{,}000$. (from Matlis et al. 2008b)

part of Fig. 32. The dark regions approximately 25% of the way in from either end are the locations of the posts that were holding the cylinder. The thin dark horizontal line is the demarcation between the two plasma actuators at the ±90° locations.

The flow behind the cylinder was made visible by introducing atomized oil particles upstream of the contraction of the open-return tri-sonic wind tunnel. The particles were made visible using a light sheet from a 5W Argon laser. The light sheet was thin in the cross-flow direction and fanned out in the flow direction. The rightmost photograph shows the particles in the wake with the plasma actuator off. The camera exposure time averages the image, with the dark region indicative of the average wake width. The wake width in the case with the plasma actuator off is indicated by the white dashed lines. When the plasma actuators are on, there is a noticeable reduction in the width of the wake, that is similar to that observed in the low-Mach-number cylinder flow visualization images in Fig. 31.

4 Further applications

The previous examples of applications of SDBD plasma actuators are a tiny representation of the ever growing number that have appeared in the literature (Corke et al. 2007b; Moreau 2007). A partial list of these includes exciting boundary layer instabilities on a sharp cone at Mach 3.5 (Kosinov et al. 1990; Corke et al. 2001; Matlis 2004), lift augmentation on a wing section (Corke et al. 2002, 2006b; Nelson et al. 2006a; Patel et al. 2006; Goeksel et al. 2006, Goeksel and Rechenberg 2004), low-pressure turbine blade separation control (Huang 2005; Huang et al. 2006a, 2006b; List et al. 2003; Suzen et al. 2007; Rizzetta and Visbal 2007; Rivir 2007), turbine tip clearance flow control (Morris et al. 2005; Douville et al. 2006; Van Ness et al. 2006), bluff body flow control (Thomas et al. 2006; Asghar et al. 2006; Do et al. 2007), turbulent boundary layer control (Wilkinson 2003; Hultgren and Ashpis 2003; Balcer et al. 2006; Porter et al. 2007), unsteady vortex generation and control (Visbal and Gaitonde 2006; Nelson et al. 2007), and airfoil leading-edge separation control (Post and Corke 2003, 2004, Post 2004; Corke et al. 2004). New applications continue to appear as more investigators gain experience in using these flow actuators. Besides a number of U.S. universities and government laboratories, there are active programs in DBD plasma flow control that we know of in Germany, France, England, Russia, Japan and China.

In addition to flow control, a new ac "plasma sensor" for velocity measurements has recently been developed by Matlis and Corke (2005). Although it was originally intended for high Mach number, high enthalpy flows, it is quite suited for low-speed flows, or applications in which harsh conditions make more conventional flow sensors unusable. A recent example of its use includes detecting traveling stall cells in a transonic compressor stage (Matlis et al. 2008a). This technology offers the unique opportunity for combined plasma actuators and sensors that could be beneficial for closed-loop feedback control in a single element.

5 Summary

The background to flow control based on the use of SDBD plasma actuators has been presented. The basis of the actuators is the generation of a body force vector that results from the combination of the local ionization of the air over the actuator, and the electric field produced by the geometric design of electrodes and dielectric layer. The dielectric layer between the electrodes is an essential part of the actuator and distinguishes it from dc-based plasma actuators, and those that rely exclusively on the dielectric properties of an air gap between the electrodes. The charge build-up on the dielectric layer provides a self-limiting capability that prevents micro-discharges from degenerating into thermal arcs. As a result, most of the energy goes into the body force, with very little thermal heating. The ionization of the air by the ac input is a highly dynamic process. Predictions of the actuator effect and its optimization, rely on a fundamental understanding of these processes. Plasma actuator simulations that make use of a combination of first principle conservation laws and computationally efficient ionization models have shown remarkable agreement with experiments, and point to improved designs and operation. Recent optimization of the actuators produced by better choices of thick dielectric materials, and ac input frequencies and waveforms have led to order of magnitude improvements in their performance compared to earlier designs that used thin Kapton film.

Simplified models have compared well to experiments at incompressible Mach numbers. Experiments to implement the effects of large variations in static pressure and gas composition are ongoing by a number of investigators. Although the actuators have been shown to be effective at supersonic Mach numbers, model validation in this regime needs to be investigated. Within the parameter space of $0 \leq M \leq 0.3$ and near-atmospheric pressures where simulations and experiments where compared, the actuator body force effect on the local flowfield was well predicted. A singular advantage of plasma actuators compared to other flow control actuators that eject fluid, is that the actuator effect is by first principles, represented as a body force. This makes investigating the parameter space in numerical flow

simulations significantly more efficient. This has a paradigm changing capability whereby numerical simulations can be used to efficiently explore aerodynamic shapes and plasma actuator arrangements that optimize performance metrics. Such a "flow control by design" approach is the ultimate potential of this technology.

References

Asghar A, Jumper EJ, Corke TC (2006) On the use of Reynolds number as the scaling parameter for the performance of plasma actuator in a weakly compressible flow AIAA Paper 2006-21

Balcer BE, Franke ME, Rivir RB (2006) Effects of plasma induced velocity on boundary layer Flow AIAA Paper 2006-875

BenGadri R, Rabehi A, Massines F, Segur P (1994) Numerical modelling of atmospheric pressure low-frequency glow discharge between insulated elecrodes. In: Proceedings of the XII ESCAMPIG, Netherlands, 23–26 August. pp 228–229

Boeuf JP (1987) Numerical model of rf glow discharges. Phys Rev A 36(6):2782–2791

Boeuf JP, Pitchford LC (2005) Electrohydrodynamic force and aerodynamic flow acceleration in surface dielectric barrier discharge. J App Phys 97

Cavalieri D (1995) On the experimental design for instability analysis on a cone at Mach 3.5 and 6.0 using a corona discharge perturbation method. Dissertation, Illinois Institute of Technology

Corke TC, Matlis E (2000) Phased plasma arrays for unsteady flow control AIAA paper 2000-2323

Corke T, Cavalieri D, Matlis E (2001) Boundary layer instability on a sharp cone at mach 3.5 with controlled input. AIAA J 40:1015

Corke TC, Jumper EJ, Post ML, Orlov D, McLaughlin TE (2002) Application of weakly-ionized plasmas as wing flow-control devices AIAA Paper 2002-0350

Corke T, He C, Patel M (2004) Plasma flaps and slats: an application of weakly-ionized plasma actuators AIAA Paper 2004-2127

Corke T, Mertz B, Patel M (2006a) Plasma flow control optimized airfoil AIAA Paper 2006-1208

Corke TC, Mertz B, Patel MP (2006b) Plasma flow control optimized airfoil AIAA paper 2006-1208

Corke T, Post M, Orlov D (2007a) Overview of plasma enhanced aerodynamics: Concepts, optimization, and applications. AIAA J Prop Power

Corke TC, Post ML, Orlov DM (2007b) Sdbd plasma enhanced aerodynamics: concepts, optimization and applications. Prog Aerosp Sci 43:193–217

Davidson G, O'Neil R (1964) Optical radiation from nitrogen and air at high pressure excited by energetic electrons. J Chem Phys 41:3946–3949

Decomps P, Massines F, Mayoux C (1994) Electrical and optical diagnosis of an atmospheric pressure glow discharge. Acta Phys Univ Com 47

Do H, Kim W, Mungal M, Capelli M (2007) Bluff body flow control using surface dielectric barrier discharges AIAA Paper 2007-0939

Douville T, Stephens J, Corke T, Morris S (2006) Turbine blade tip leakage flow control by partial squealer tip and plasma actuators AIAA Paper 2006-20

Eliasson B, Kogelschatz U (1991) IEEE Trans Plasma Sci 19:309

Enloe L, McLaughlin T, VanDyken, Kachner, Jumper E, Corke T (2004a) Mechanisms and responses of a single-dielectric barrier plasma actuator: plasma morphology AIAA 42:589–594

Enloe L, McLaughlin T, VanDyken, Kachner, Jumper E, Corke T, Post M, Haddad O (2004b) Mechanisms and responses odf a single-dielectric barrier plasma actuator: geometric effects. AIAA 42:595–604

Falkenstein Z, Coogan J (1997) Microdischarge behaviour in the silent discharge of nitrogen-oxygen and water-air mixtures. J Phys D App Phys 30:817–825

Font G (2004) Boundary layer control with atmospheric plasma discharges. AIAA Paper 2004-3574

Font G, Morgan WL (2005) Plasma discharges in atmospheric pressure oxygen for boundary layer separation control. AIAA paper 2005-4632

Forte M, Jolibois J, Moreau F, Touchard G, Cazalens M (2006) Optimization of a dielectric barrier discharge actuator by stationary and non-stationary measurements of the induced flow velocity—application to flow control. 3rd AIAA flow control conference, AIAA Paper 2006-2863

Gaitonde D, Visbal M, Roy S (2005a) Control of flow past a wing section with plasma-based body forces. AIAA paper 2005-5302

Gaitonde DV, Visbal MR, Roy S (2005b) Contol of flow past a wing section with plasma-based body forces. AIAA Paper 2005-5302

Gibalov V, Pietsch G (2000a) The development of dielectric barrier discharges in gas gaps and surfaces. J Phys D Appl Phys 33:2618

Gibalov V, Pietsch G (2000b) The development of dielectric barrier discharges in gas gaps and on surfaces J Phys D 33

Goeksel B, Rechenberg I (2004) Active separation flow control experiments in weakly ionized air. In: 10th EUROMECH European Turbulence Conference, Barcelona

Goeksel B, Rechenberg I, Greenblatt D, Paschereit C (2006) Steady and unsteady plasma wall jets for separation and circulation control. AIAA Paper 2006-3686

Golubovskii Y, Maiorov V, Behnke J, Behnke J (2002) Influence of interaction between charged particles and dielectric surface over a homogeneous barrier discharge in nitrogen. J Phys D Appl Phys 35

Greenblatt D, Paschal K, Schaeffler N, Washburn A, Harris J, Yao C (2004) A separation control cfd validation test case. part 1: baseline and steady suction. AIAA Paper 2004-2220

He C (2008) SDBD Plasma actuator separation control. Dissertation, University of Notre Dame

He C, Corke TC, Patel M (2007) Numerical and experimental analysis of plasma flow control over a hump model. AIAA paper 2007-0935

Huang J (2005) Documentation and control of flow separation on a linear cascade of Pak-B blades using plasma actuators. Dissertation, University of Notre Dame

Huang J, Corke T, Thomas F (2006a) Plasma actuators for separation sontrol of low pressure turbine blades. AIAA J 44:51

Huang J, Corke T, Thomas F (2006b) Unsteady plasma actuators for separation control of low-pressure turbine blades AIAA J 44:1477

Hultgren LS, Ashpis DE (2003) Demonstration of separation delay with glow-discharge plasma actuators. AIAA Paper 2003-1025

Iqbal M, Corke T, Thomas F (2007) Parametric optimization of single dielectric barrier discharge (sdbd) plasma actuators submitted. AIAA J

Kakuta S, Kamata T, Makabe T, Kobayashi S, Terai K, Tamagawa T (1995) Study of surface charges on dielectric electrodes in a radio-frequency glow discharge. J Appl Phys 77

Kanazawa S, Kogoma M, Moriwaki T, Okazaki S (1988) Stable glow plasma at atmospheric pressure. J Phys D Appl Phys 21:836

Kanazawa S, Kogoma M, Okazaki S, Moriwaki T (1989) Glow plasma treatment at atmospheric presure for surface modification and film deposition. Nuclear Inst Methods Phys Res B37:842

Kanzawa S, Kogoma M, Kanazawa S, Moriwaki T, Okazaki S (1990) The improvement of atmospheric-pressure glow plasma method and the deposition of organic films. J Phys D Appl Phys 23:374

Kline M, Miller N, Walhout M (2001) Time-resolved imaging of spatiotemporal patterns in a one-dimensional dielectric-barrier discharge system. Phys Rev E 64:26402–1

Kogelschatz U (1977) In: Proceedings of the international conference on phenomena ionized gases, ICPIG XXIII, Tolouse, FR

Kogoma M, Okazaki S (1994) Raising of ozone formation efficiency in a homogeneous glow discharge plasma at atmospheric pressure. J Phys D Appl Phys 27:1985

Kosinov A, Maslov A, Shevelkov S (1990) Experiments on the stability of supersonic laminar boundary layers. J Fluid Mech 219: 621

Kozlov K, Wagner H-E, Brandenburg R, Michel P (2001) Spatio-temporally resolved spectroscopic diagnostics of the barrier discharge in air at atmosperic pressure. J Phys D Appl Phys 34

Kunhardt E (1980) Electrical breakdown of gases: the pre-breakdownstage. IEEE Trans Plasma Sci PS-8:234

Kunhardt E (2000) Generation of large volume atmospheric pressure nonequilibrium plasmas. IEEE Trans Plasma Sci 28(1): 189–199

Kunhardt E, Luessen L (1981) Electrical breakdown and discharges. Plenum, New York

Landau LD, Lifshitz, E (1984) Electrodynamics of continuous media Pergamon

Langmuir I (1926) Proc Nat Acad Sci 14:627

Likhanskii A, Shneider M, Macheret S, Miles R (2006) Modeling of interaction between weakly ionized near-surface plasmas and gas flow. AIAA Paper 2006-1204

List J, Byerley AR, McLaughlin TE, VanDyken RD (2003) Using a plasma actuator to control laminar separation on a linear cascade turbine blade. AIAA Paper 2003-1026

Llewellyn-Jones F (1966) The glow discharge and an introduction to plasma physics, Methuen, New York, USA

Madani M, Bogaerts A, Gijbels R, Vangeneugden D (2003) Modelling of a dielectric barrier glow discharge at atmospheric pressure in nitrogen. In: International conference on phenomena in ionized gases

Massines F, Ghadri R, Decomps P, Rabehi A, Segur P, Mayoux C (1995) Atmospheric pressure dielectric controlled glow discharges: diagnostics and modelling. In: Proceedings of the international conference on phenomena ionized gases, ICPIG XXII, Hoboken, NJ, p 306

Massines F, Rabehi A, Decomps P, Ben Gadri R, Segur P, Mayoux C (1998a) Experimental and theoretical study of a glow discharge at atmosperic pressure controlled by dielectric barrier. J Appl Phys 83

Massines F, Rabehi A, Descomps P, Gadri R, Segur P, Mayoux C (1998b) Mechanisms of a glow discharge at atmospheric pressure controlled by dielectric barrier. J Appl Phys 83-86:2950

Matlis EH (2004) Controlled experiments on instabilities and transition to turbulence on a sharp cone at Mach 3.5. Dissertation, University of Notre Dame

Matlis E, Corke T (2005) AC plasma anemometer for hypersonic Mach number experiments. AIAA Paper 2005-0952

Matlis E, Corke T, Cameron J, Morris S (2008a) A.c. plasma anemometer for axial compressor stall warning. 12th international symposium on transport phenomena and dynamics of rotating machines, 17–22 February

Matlis E, Corke T, Gogineni S (2008b) Private communications, University of Notre Dame

Meek J, Craggs JDE (1978) Electrical breakdown of gases. Wiley, Chichester

Moreau E (2007) Airflow control by non-thermal plasma actuators J Phys D Appl Physics 40:605–636

Morris SC, Corke TC, VanNess D, Stephens J, Douville T (2005) Tip clearance control using plasma actuators. AIAA paper 2005-0782

Nasser E (1971) Fundamentals of gaseous ionization and plasma electronics, Chap. 12. Wiley, New York

Naude N, Cambronne J-P, Gherardi N, Massines F (2004) Electrical model of an atmospheric pressure townsend-like discharge (aptd). Eur Phys J Appl Phys (November 2004) 1–7

Nelson C, Cain A, Patel M, Corke T (2006a) Simulation of plasma actuators using the wind-US code. AIAA Paper 2006-634

Nelson C, Cain A, Patel M, Corke T (2006b) Simulation of plasma actuators using the wind-US code. AIAA Paper 2006-0634

Nelson R, Corke T, Patel M, Ng T (2007) Modification of the flow structure over a UAV wing for roll control. AIAA Paper 2007-0884

Okazaki S, Kogoma M, Uehara M, Kimura Y (1993) Appearance of stable glow discharge in air, argon oxygen, and nitrogen at atmospheric pressure using 50 hz source. J Phys D Appl Phys 26:889

Orlov DM (2006) Modelling and simulation of single dielectric barrier discharge plasma actuators. Dissertation, University of Notre Dame

Orlov D, Corke T (2005) Numerical simulation of aerodynamic plasma actuator effects. AIAA Paper 2005-1083

Orlov D, Corke T, Haddad O (2003) DNS modeling of plasma array flow actuators. In: Bulletin of the American Physical Society Division of Fluid Dynamics, vol 48

Orlov D, Corke T, Patel M (2006) Electric circuit model for aerodynamic plasma actuator. AIAA Paper 2006-1206

Pai S, Guo X, Zhou T (1996) Closed form analytic solution describing glow discharge plasma. Phys Plasmas 3

Pashaie B, Dhali S, Honea F (1994) Electrical characteristics of a coaxial dielectric barrier discharge. J Phys D Appl Phys 27:2107

Patel MP, Sowle ZH, Corke TC, He C (2006) Autonomous sensing and control of wing stall using a smart plasma slat. AIAA Paper 2006-1207

Patel M, Ng T, Vasudevan S, Corke T, He S (2007a) Aerodynamic control using windward-surface plasma actuators on a separation ramp. J Aircraft 44(6):1889–1895

Patel M, Ng T, Vasudevan S, Corke T, He S (2007b) Plasma actuators for hingeless aerodynamic control of an unmanned air vehicle. J Aircraft 44(4):1264–1274

Patel M, Ng T, Vasudevan S, Corke T, Post M, McLaughlin T, Suchomel C (2008) Scaling effects of an aerodynamic plasma actuator. J Aircraft 45(1):223–236

Paulus M, Stals L, Rude U, Rauschenbach B (1999) Two-dimensional simulation of plasma-based ion implantation J Appl Phys 85

Poggie J (2005) DC glow discharges: a computational study for flow control applications. AIAA Paper 2005-5303

Porter C, Baughn J, McLaughlin T, Enloe C, Font G (2006) Temporal force measurements on an aerodynamic plasma actuator. AIAA Paper 2006-104

Porter C, McLaughlin T, Enloe L, Font G (2007) Boundary layer control using DBD plasma actuator. AIAA Paper 2007-0786

Post ML (2001) Phased plasma actuators for unsteady flow control. Dissertation, M.S. in Aerospace and Mechanical Engineering, University of Notre Dame

Post ML (2004) Plasma actuators for separation control on stationary and unstationary airfoils. Dissertation, University of Notre Dame

Post ML, Corke TC (2003) Separation control on high angle of attack airfoil using plasma actuator. AIAA Paper 2003-1024

Post ML, Corke TC (2004) Separation control using plasma actuators—stationary and oscillatory airfoils. AIAA Paper 2004-0841

Post M, Corke T (2004) Separation control on high angle of attack airfoil using plasma actuators. AIAA J 42:2177

Post M, Erturk E, Corke T (2001) Phased plasma arrays for unsteady flow control. In: Bulletin of the American Physical Society Division of Fluid Dynamics, vol 46

Rabehi A, BenGadri R, Segur P, Massines F, Decomps P (1994) Numerical modelling of high pressure glow discharges controlled by dielectric barrier. In: Proceedings of the converence on electrical insulation and dielectric phenomena, Arlington, TX, 23–26 October, 1994, pp 840–845

Raizer Y (1991) Gas discharge physics. Springer, Berlin

Rivir R (2007) Effects of pulsed dc discharge plasma actuators in a separated LPT boundary layer. AIAA Paper 2007-0942

Rizzetta D, Visbal M (2007) Numerical investigation of plasma-based flow control for a transitional highly-loaded low-pressure turbine. AIAA Paper 2007-0938

Roth J (1995a) Industrial plasma engineering. Inst Phys Publishing, Philadelphia

Roth J (1995b) Industrial plasma engineering Institute of Physics Publishing

Roth J, Sherman D, Wilkinson S (1998) Boundary layer flow control with one atmosphere uniform glow discharge surface plasma. AIAA Paper 1998-0328

Roth J, Sherman D, Wilkinson S (2000) Electrohydrodynamic flow control with a glow-discharge surface plasma. AIAA Journal 38

Roy S, Gaitonde DV (2004) Radio frequency induced ionized collisional flow model for application at atmospheric pressures. J Appl Phys

Roy S, Gaitonde DV (2005) Modeling surface discharge effects of atmospheric RF on gas flow control. AIAA Paper 2005-0160

Roy S, Pandey B, Poggie J, Gaitonde DV (2003) Modeling low pressure collisional plasma sheath with space-charge effect. Phys Plasmas 10:2578–2585

Shyy W, Jayaraman B, Andersson A (2002) Modeling of glow discharge-induced fluid dynamics. J Appl Phys 92

Suzen Y, Huang P (2006) Simulation of flow separation control using plasma actuators. AIAA paper 2006-877

Suzen Y, Huang P, Jacob J, Ashpis D (2005) Numerical simulations of plasma based flow control applications. AIAA Paper 2005-4633

Suzen Y, Huang G, Ashpis D (2007) Numerical simulations of flow separation control in low-pressure turbines using plasma actuators. AIAA Paper 2007-0937

Thomas FO, Kozlov A, Corke TC (2006) Plasma actuators for bluff body flow control. AIAA paper 2006-2845

Thomas F, Kozlov A, Corke T (2008) Plasma actuators for bluff body flow control. AIAA J (in press)

Trunec D, Brablec A, Stastny F (1998) Contrib Plasma Phys 38:435

Van Ness DK, Corke TC, Morris SC (2006) Turbine tip clearance flow control using plasma actuators. AIAA Paper 2006-21

Vidmar R, Stalter K (2003) Air chemistry and power to generate and sustain plasma: plasma lifetime calculations. AIAA Paper 2003-1189

Visbal MR, Gaitonde DV (2006) Control of vortical flows using simulated plasma actuators. AIAA Paper 2006-505

Voikov V, Corke T, Haddad O (2004) Numerical simulation of flow control over airfoils using plasma actuators. In: Bulletin of the American Physical Society Division of Fluid Dynamics, vol 49

Wilkinson SP (2003) Investigation of an oscillating surface plasma for turbulent drag reduction. AIAA Paper 2003-1023

Yokoyama T, Kogoma M, Moriwaki T, Okazaki S (1990) The mechanism of the stabilization of glow plasma at atmospheric pressure. J Phys D Appl Phys 23:1125